A kinetic model of a polyelectrolyte gel undergoing phase separation

Giulia L. Celora[a,*], Matthew G. Hennessy[a,c], Andreas Münch[a], Barbara Wagner[b], Sarah L. Waters[a]

[a] *Mathematical Institute, Woodstock Road, University of Oxford, Oxford, OX2 6GG, UK*
[b] *Weierstrass Institute, Mohrenstrasse 39, 10117 Berlin, Germany*
[c] *Department of Engineering Mathematics, University of Bristol, University Walk, Bristol, BS8 1TW, UK*

Abstract

In this study we propose a novel phase-field theory based on non-equilibrium thermodynamics that resolves both the macroscopic deformations and the internal structure of a polyelectrolyte gel immersed in an ionic solution. The governing equations for the gel account for its electro-chemical response, the nonlinear elasticity of its polyelectrolyte network, multi-component Stefan–Maxwell diffusion and the energy cost of internal interfaces that form upon phase separation. These equations are coupled to a hydrodynamic model for the surrounding ionic solution. The full time-dependent model describes the evolution of the gel-solution system across multiple time and spatial scales revealing the mechano-electro-chemical mechanisms that regulate phase separation of the gel, which results in the emergence of complex spatial patterns. The rich dynamics of this system are investigated for a constrained gel undergoing uni-axial deformations. We find that the regulation of phase separation in the gel-bath system is dependent on the competition between two physical length scales: the Kuhn and Debye lengths which characterise the thickness of electric double layers and diffuse interfaces, respectively. When the Kuhn length is much larger than the Debye length, the standard electroneutral assumption can be invoked. In this case, we show that large-scale solvent flux can result in the phase separation of the gel. Depending on the concentration of ions in the surrounding bath, swelling/deswelling of the gel occurs either via propagation of a front from the gel-bath interface or via front propagation combined with spinodal decomposition. In the limit where the Kuhn and Debye length are commensurate, our model predicts a novel mode of phase separation which results in the gel bulk organising into spatially localized stable charged domains that emanate from the Debye layer and propagate through the whole gel.

Keywords: polyelectrolyte gel, phase separation, volume phase transition, cross diffusion, electric double layer

1. Introduction

A polyelectrolyte gel is a network of covalently cross-linked polyelectrolyte macromolecules that is swollen with a fluid. The polyelectrolyte chains are electrically charged and they interact with dissolved ions in the imbibing fluid. If placed in a salt solution, hereafter referred to as an *ionic bath*, chemical, electrical, and mechanical interactions occur within the gel that drive it towards an equilibrium state. Applying a stimulus such as an electric field or a temperature change enables the equilibrium state of the gel to be finely controlled. The evolution of the gel towards its equilibrium has been the subject of numerous theoretical and experimental studies [1–7] which have unveiled a plethora of phenomena including the volume phase transitions [8–10], super-collapse [11, 12], and re-entrant swelling [13]. The volume phase transition, which leads to enormous and discontinuous changes in the gel volume, has received considerable attention due to its relevance in stimuli-responsive smart materials and sensors [14–17].

When considering the transient evolution of the gel between different equilibria, internal structures can emerge via phase separation, whereby regions of highly swollen and collapsed gel spontaneously appear and co-exist. These highly and weakly swollen phases are separated by diffuse interfaces with a small thickness that is characterised by the Kuhn length of the macromolecules. As shown experimentally by Tanaka *et al.* [9, 18], phase separation gives rise to surface instabilities which can transiently or permanently affect the gel morphology and its resulting properties. Environmental changes of the gel may also result in micro- or nano-phase separation [19, 20] or reverse Ostwald ripening [21, 22]. These features play an important role in many biological processes such as in subcellular organelle formation [23, 24].

Near the interface between a polyelectrolyte gel and an ionic bath, ions from the bath accumulate to screen the electric charges on the polyelectrolyte macromolecules. This gives rise to a diffuse layer of charge known as the electric double layer. However, due to the porous nature of the gel, ions in the imbibing fluid will, in turn, accumulate to screen the diffuse layer of charge outside of the gel. Thus, the electric double layer in gel-bath systems are doubly diffuse [25]. Furthermore, due to the concentration of ions being different inside and outside of the gel, the electric

*Corresponding author

Email addresses: celora@maths.ox.ac.uk (Giulia L. Celora), matthew.hennessy@bristol.ac.uk (Matthew G. Hennessy), muench@maths.ox.ac.uk (Andreas Münch), Barbara.Wagner@wias-berlin.de (Barbara Wagner), waters@maths.ox.ac.uk (Sarah L. Waters)

double layer is asymmetric. In particular, the thickness of the charged layer, as characterised by the Debye length, is often greater in the gel than in the bath. The amount of charge in the electric double layer typically decreases with distance from the gel-bath interface until the gel and the bath become electrically neutral.

Although extensive theoretical and experimental studies have revealed key insights into the behaviour of polyelectrolyte gels, several important questions remain unanswered. For example, it is not clear how the structure of a polyelectrolyte gel self-organises during the volume phase transition, as experiments often focus on the time evolution of bulk properties such as the gel size [26]. Similarly, the link between microscopic pattern formation and macroscopic observables is not established. There are also very few studies of the electric double layer in gel-bath systems [25, 27]. The conventional view is that the double layer plays a passive role in the gel dynamics; as a result, it is often neglected in modelling studies. However, the stimuli that trigger the volume phase transition are often applied to the bath and are therefore transmitted to the gel via the electric double layer. From this point of view, the double layer should play a fundamental role in setting the global structure of the gel. Moreover, if the Debye and Kuhn lengths are commensurate, then a non-trivial interplay could arise between the Coulomb interactions that structure the electric double layer and the intermolecular interactions responsible for phase separation. Such an interplay has the potential to drive a novel mode of pattern formation within the gel, but this is yet to be explored.

Motivated by these questions, we use non-equilibrium thermodynamics to derive a novel phase-field model for a polyelectrolyte gel that can capture the spontaneous formation of internal interfaces due to the onset of phase separation. Moreover, we present a thermodynamically consistent model of the surrounding ionic bath. Coupling the gel and bath models via appropriate interfacial conditions provides a means of resolving the electric double layer and elucidating the role it plays in the gel dynamics. In addition, our model captures multi-component diffusive transport using the Stefan–Maxwell formulation [28, 29] to avoid anomalous diffusivities which can arise when the diffusive flux of a species is solely driven by the gradient of its own chemical potential [30]. The Stefan–Maxwell approach correctly captures the hydrodynamic drag between different components of the mixture by balancing the friction forces between the different species [31]. While having been previously ignored for polyelectrolyte gels [27], the recent work by Zhang et al. [32] has highlighted

the role of cross-diffusion in modelling effects such as a temporary excess of salt entering the gel during swelling, which is subsequently rejected as the gel approaches its new equilibrium.

Our analysis reveals that the structure of the gel is crucially dependent on the ratio of the Debye length to the Kuhn length. When the Debye length is much smaller than the Kuhn length, then the equilibrium states correspond to a gel that has a homogeneous and electrically neutral bulk with a thin electric double layer at its free surface. In this case, the electric double layer is passive and does not affect the dynamics, in line with previous studies. By simulating the volume phase transition in this regime, we find that it can occur via two distinct routes, either solely via the propagation of a swelling/deswelling front from the gel-bath interface or in combination with spinodal decomposition ahead of the main transition front. When the Debye and Kuhn lengths are commensurate, our model predicts a novel mode of pattern formation, resulting in stable, spatially localized structures that emanate from the electric double layer and invade the gel. In this case, the equilibrium states of the gel can be non-homogeneous and electrically charged. We show that this novel model of pattern formation arises due to the interplay between phase separation and the formation of electric double layers and can be detected through measurements of the gel size.

The paper is organised as follows. In Sections 2 and 3, we present the governing equations for a polyelectrolyte gel and the surrounding ionic bath, respectively. The interfacial conditions that couple these models are discussed in Section 4. In Section 5 we use one-dimensional simulations to analyse and interpret structure formation within the gel. Finally, we provide a conclusion and outlook in Section 6.

2. Model derivation for a polyelectrolyte gel

We consider the gel as a multi-component material composed of a solid polymer network with fixed charges and a solution consisting of solvent, such as water, and N freely moving ionic species (i.e. solutes), see Figure 1. We assume all phases are intrinsically incompressible and isotropic. Throughout the model derivation, we use subscripts n, s to denote the solid polymer network and solvent respectively, the index $i \in \{1, \dots, N\}$ to denote the ionic species, and the index $m \in \{s, 1, \dots, N\}$ to refer to the species that are mobile relative to the network, i.e. both the solvent and solutes. For later convenience, we introduce the set notation $\mathbb{I} = \{1, \dots, N\}$ and $\mathbb{M} = \{s, 1, \dots, N\}$.

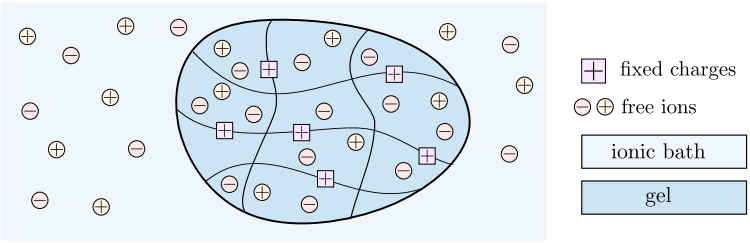

Figure 1: Schematic representation of a polyelectrolyte gel in contact with an ionic bath. The gel is a three-phase material, composed of a solid polymer network with fixed charges, solvent, and freely moving ions. The ionic bath consists of solvent and freely moving ions.

The model is derived using standard arguments from thermodynamics. We start by setting up the kinematics, followed by the conservation laws and electrostatics for the system; we then construct the free energy of the system and use the energy imbalance inequality of Gurtin [33] to obtain thermodynamically consistent expressions for the constitutive equations. The mass fluxes are then determined assuming the system is near equilibrium and that Stefan-Maxwell cross-diffusion takes place.

2.1. Kinematics

The motivation for this study is to understand the swelling/deswelling behaviour of a polyelectrolyte gel in contact with an ionic bath. By changing the conditions in the bath, such as the concentration of ions, the polyelectrolyte gel will swell or shrink. To capture this behaviour, we consider a gel that is initially pre-swollen and in equilibrium with the surrounding bath. We then alter the conditions in the bath to drive the gel towards a new equilibrium state. The initial configuration will differ from the reference state, the latter of which is stress free and assumed to be the dry gel, i.e. with only the solid phase is present; see Figure 2.

We adopt standard notation in continuum mechanics. The smooth function $\boldsymbol{\chi}$ is a one-to-one map between material points in the reference configuration $\boldsymbol{X} \in \mathcal{B}_R$ to points $\boldsymbol{x} = \boldsymbol{\chi}(\boldsymbol{X}, t)$ (Eulerian coordinates) in the current configuration $\mathcal{B}_t$. The deformation gradient tensor is then defined by $\mathbf{F} = \partial\boldsymbol{\chi}/\partial\boldsymbol{X}$, where $J = \det \mathbf{F} > 0$ encodes information about the change in volume during deformation. We further introduce the displacement vector $\boldsymbol{u} = \boldsymbol{x} - \boldsymbol{X}$. As the gel deformation is determined by the displacement of the solid phase, the solid phase velocity, $\boldsymbol{v}_n$, and displacement are related, so that $\boldsymbol{v}_n = \dot{\boldsymbol{u}}$, where dots denote derivatives with respect to time in the reference configuration, i.e. $\partial/\partial t|_{\boldsymbol{X}}\, \boldsymbol{u}$.

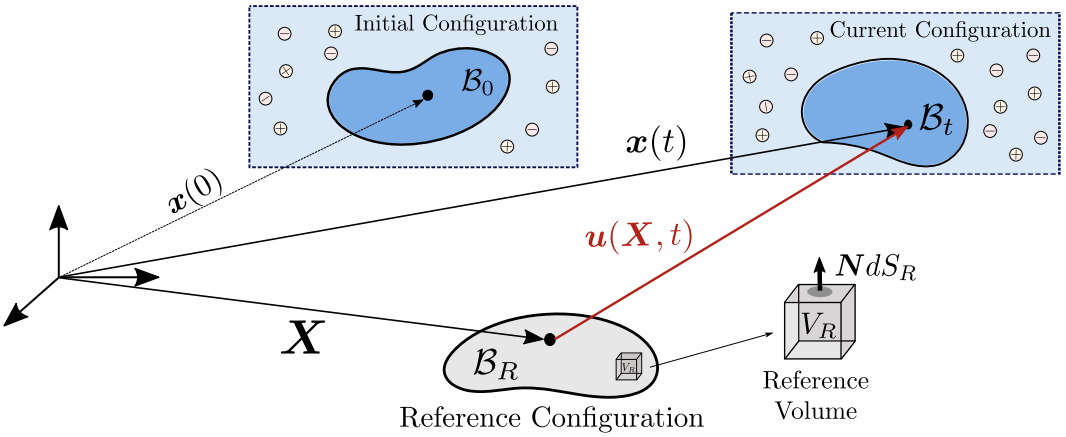

Figure 2: Sketch of the reference, initial and current state of the gel.

2.2. Conservation equations and electrostatics

As the solid phase is incompressible, any change in volume during deformation is due to the migration of solvent and solute molecules, whose nominal concentrations (i.e. number of molecules per unit volume in $\mathcal{B}_R$) are denoted by $C_m = C_m(\boldsymbol{X}, t)$ $(m \in \mathbb{M})$. This leads to the molecular incompressibility condition:

$$J = 1 + \sum_{m \in \mathbb{M}} \nu_m C_m, \tag{1a}$$

where ν_m $(m \in \mathbb{M})$ is the molecular volume of each species in the solution.

Conservation of each mobile species in the reference configuration reads as

$$\dot{C}_m + \nabla_R \cdot \boldsymbol{J}_m = 0, \tag{1b}$$

where $\boldsymbol{J}_m = \boldsymbol{J}_m(\boldsymbol{X}, t)$ is the nominal flux per unit area in the reference state and ∇_R denotes the gradient with respect to the Lagrangian coordinates $\boldsymbol{X}$.

When considering gels, inertial and gravitational effects are commonly neglected, so that the conservation of momentum is given by

$$\nabla_R \cdot \mathbf{S} = \mathbf{0}, \tag{1c}$$

where $\mathbf{S} = \mathbf{S}(\boldsymbol{X}, t)$ is the first Piola–Kirchhoff tensor, which represents the stress state of the polyelectrolyte gel in the reference configuration.

The accumulation of electric charges generates an electric field which is denoted by $\boldsymbol{E} = \boldsymbol{E}(\boldsymbol{X}, t)$ in the reference configuration. While the gel as whole is a conductor due to the motion of the free

ions in the solution, following Refs [16, 34–36] we treat the solid network and the solvent as linear dielectric materials. Consequently, Maxwell's equations in the reference configuration reads:

$$\boldsymbol{E} = -\nabla_R \Phi, \tag{1d}$$

$$\nabla_R \cdot \boldsymbol{H} = Q, \tag{1e}$$

where $\Phi = \Phi(\boldsymbol{X}, t)$ is the electrostatic potential, $\boldsymbol{H} = \boldsymbol{H}(\boldsymbol{X}, t)$ is the nominal electric displacement, and $Q = Q(\boldsymbol{X}, t)$ is the nominal total charge density. The latter accounts for both fixed and moving charges and it is therefore defined as

$$Q = e\left(\sum_{i\in\mathbb{I}} z_i C_i + z_f C_f\right), \tag{1f}$$

where e is the elementary charge; C_f is the nominal concentration of fixed charges on the polyelectrolyte chains; and z_i is the valence of the corresponding charged species.

2.3. Free energy

Equations of state that are consistent with the second law of thermodynamics can be derived by specifying the free energy per unit volume in the reference configuration Ψ. We assume that the free energy is separable into five contributions as follows:

$$\Psi = \Psi_1(\mathbf{F}, \boldsymbol{H}) + \Psi_2(C_m) + \Psi_3(C_m) + \Psi_4(\boldsymbol{F}) + \Psi_5(\nabla_R C_s, \nabla_R J). \tag{2}$$

The free energy of polarisation, Ψ_1, is given by [16, 34, 35]:

$$\Psi_1 = \frac{1}{2\epsilon J}\,\mathbf{F}\boldsymbol{H}\cdot\mathbf{F}\boldsymbol{H}. \tag{3}$$

In Eq. (3) the permittivity ϵ is in general a function of the solvent concentration [27]. However, we assume that the permittivity is dominated by the contribution from the solvent so that ϵ is independent of the gel composition.

The second term in the free energy, Ψ_2, captures the energetic contributions of the pure mobile species and it has the standard form [37]:

$$\Psi_2 = \sum_{m\in\mathbb{M}} \mu_m^0 C_m, \tag{4}$$

where μ_m^0 denotes the chemical potential of non-interacting mobile species.

The third term Ψ_3 describes the free energy of mixing. We assume that the leading contribution to the enthalpy is due to disfavourable interactions between the solvent and the hydrophobic solid phase [38]. According to the Flory–Huggins theory [39, 40] of solvent-polymer mixtures, the mixing energy Ψ_3 is then given by

$$\Psi_3 = k_B T \left(\frac{\chi C_s}{1 + \sum_{j \in \mathbb{M}} \nu_j C_j} + \sum_{m \in \mathbb{M}} C_m \ln \frac{\nu_m C_m}{1 + \sum_{j \in \mathbb{M}} \nu_j C_j} \right), \tag{5}$$

where k_B is Boltzmann's constant, T is the temperature, and χ is the Flory interaction parameter (capturing the enthalpy of mixing the solvent and solid phase).

The elastic energy due to the stretching of the polymer network is described by Ψ_4. We assume that the elastic response of the network is captured by a neo-Hookean strain energy density of the form

$$\Psi_4 = \frac{G}{2} \left(\mathbf{F} : \mathbf{F} - 3 - 2 \ln J \right). \tag{6}$$

where G is the shear modulus.

The fifth and final contribution to the free energy, Ψ_5, captures the energy cost associated with internal interfaces that form within the gel due to phase separation. We assume that the ionic concentrations are dilute and that the dominant contribution to the interfacial free energy arises from gradients in the solvent concentration. However, our theory could easily accommodate more general forms of the interfacial free energy that depend on gradients of all of the species [41]. In the current configuration, we consider the specific form of $\psi_5 = \Psi_5 / J = \gamma / 2 \left| \nabla c_s \right|^2$, where γ plays a role analogous to surface tension [42]. Following Wu *et al.* [43], we relate the parameter γ to the Kuhn length, L_K, of the network via the relation $\gamma = k_B T \nu_s L_K^2$. By expressing ψ_5 in the reference configuration, we find that Ψ_5 has the form

$$\Psi_5 = \frac{\gamma}{2J} G_{iJ} G_{iM} \frac{\partial C_s}{\partial X_J} \frac{\partial C_s}{\partial X_M} + \frac{\gamma C_s^2}{2J^3} G_{iJ} G_{iM} \frac{\partial J}{\partial X_J} \frac{\partial J}{\partial X_M} - \frac{\gamma C_s}{J^2} G_{iJ} G_{iM} \frac{\partial C_s}{\partial X_J} \frac{\partial J}{\partial X_M}, \tag{7}$$

where $\mathbf{G} = \mathbf{F}^{-T}$ and summation over repeated indices is implied. We note that Eq. (7) is just one of the possible choices for the interfacial free energy in solid-like systems; for other formulations we refer the reader to Hong and Wang [44].

2.4. Energy imbalance inequality

As derived by Gurtin [33, 45] when considering isothermal processes, the second law of thermodynamics can be rewritten in terms of the Helmholtz free energy Ψ to lead to the so called *energy*

imbalance inequality. More precisely, considering an arbitrary control volume in the reference configuration, $\mathcal{V}_R$, the energy imbalance inequality states that the rate of change of the net free energy in $\mathcal{V}_R$ must be less or equal to the power expended on $\mathcal{V}_R$ plus the energy increase due to the change in the species concentration from transport. Here we augment the energy imbalance to weakly impose the incompressibility condition (1a) via the Lagrange multiplier p, which plays the role of the thermodynamic pressure. For the specific system considered, we can write the energy imbalance inequality as,

$$\begin{aligned}\frac{\mathrm{d}}{\mathrm{d}t}\left\{\int_{\mathcal{V}_R}\left[\Psi - p\left(J-1-\sum_{m\in\mathbb{M}}\nu_m C_m\right)\right]dV_R\right\} \leq & -\sum_{m\in\mathbb{M}}\int_{\mathcal{S}_R}\mu_m\,\boldsymbol{J}_m\cdot\boldsymbol{N}\,dS_R \\ & -\int_{\mathcal{S}_R}\Phi\,\dot{\boldsymbol{H}}\cdot\boldsymbol{N}dS_R+\int_{\mathcal{S}_R}\mathbf{S}\boldsymbol{N}\cdot\dot{\boldsymbol{u}}\,dS_R+\int_{\mathcal{S}_R}\left[(\boldsymbol{\xi}_s\cdot\boldsymbol{N})\dot{C}_s+(\boldsymbol{\xi}_J\cdot\boldsymbol{N})\,\dot{J}\right]dS_R,\end{aligned} \tag{8}$$

where $\boldsymbol{N}dS_R$ is the surface element in $\mathcal{B}_R$ (see Fig. 2). In writing (8), we have assumed the control volume is not at the boundary between the polyelectrolyte gel and surrounding ionic solution. The first term on the right-hand side of (8) accounts for the total gain in energy due to the mass transport, where we denote by μ_m the chemical potentials of the species $m \in \mathbb{M}$. The second term in (8) captures the electrical work expended on $\mathcal{V}_R$ by the potential Φ; see Drozdov *et al.* [46] for more details. The last two integrals are the mechanical work expended on the reference volume. Following Refs [45, 47], the mechanical work is decomposed into contributions from the macro-stresses $\mathbf{S}$ and the micro-stresses $\boldsymbol{\xi}$, the latter of which originate from composition gradients.

The interfacial free energy (7) involves gradients of the solvent concentration and the Jacobian determinant, $\nabla_R C_s$ and $\nabla_R J$, resulting in micro-stresses $\boldsymbol{\xi}_s$ and $\boldsymbol{\xi}_J$, respectively. In previous works on phase separation in non-ionic hydrogels [47], the absence of free ions allowed $\nabla_R J$ to be written as $\nu_s \nabla_R C_s$. The mechanical work associated with changes in composition could then be captured through a single micro-stress $\boldsymbol{\xi}_s$. For a polyelectrolyte, however, $\nabla_R J$ and $\nabla_R C_s$ vary independently, necessitating the additional micro-stress $\boldsymbol{\xi}_J$ due to the gradient in J. Alternatively, we could have written $\nabla_R J = \sum_{m\in\mathbb{M}} \nu_m \nabla_R C_m$ and considered $\nabla_R C_m$ as independent variables, but this choice is more algebraically complicated and would have resulted in the introduction of additional micro-stresses.

The local form of the energy imbalance can be obtained from Eq. (8) by using the divergence

theorem and Eqs. (1b)-(1e) to find

$$\begin{aligned}\dot{\Psi} + \sum_{i\in\mathbb{I}} \left[e\Phi z_i - \mu_i + \nu_i p\right] \dot{C}_i - \left(\mu_s - \nu_s p + \nabla_R \cdot \boldsymbol{\xi}_s\right) \dot{C}_s - \boldsymbol{\xi}_s \cdot \nabla_R \dot{C}_s - \boldsymbol{\xi}_J \cdot \nabla_R \dot{J} \\ - \left(\mathbf{S} + pJ\mathbf{F}^{-T} + J\left(\nabla_R \cdot \boldsymbol{\xi}_J\right)\mathbf{F}^{-T}\right) : \dot{\mathbf{F}} - \boldsymbol{E} \cdot \dot{\boldsymbol{H}} + \sum_{m\in\mathbb{M}} \nabla_R \mu_m \cdot \boldsymbol{J}_m \leq 0,\end{aligned} \tag{9}$$

By writing $\Psi = \Psi(C_m, \mathbf{F}, \boldsymbol{H}, \nabla_R C_s, \nabla_R J)$ according to the energy decomposition in (2), the local energy imbalance inequality in (9) becomes

$$\begin{aligned}\left(\frac{\partial \Psi}{\partial \nabla_R C_s} - \boldsymbol{\xi}_s\right) \cdot \nabla_R \dot{C}_m + \left(\frac{\partial \Psi}{\partial C_s} - \mu_s - \nabla_R \cdot \boldsymbol{\xi}_s + \nu_s p\right) \dot{C}_s + \left(\frac{\partial \Psi}{\partial \boldsymbol{H}} - \boldsymbol{E}\right) \cdot \dot{\boldsymbol{H}} \\ + \left(\frac{\partial \Psi}{\partial \nabla_R J} - \boldsymbol{\xi}_J\right) \cdot \nabla_R \dot{J} + \sum_{i\in\mathbb{I}} \left(\frac{\partial \Psi}{\partial C_i} + e\Phi z_i - \mu_i + \nu_i p\right) \dot{C}_i \\ + \left(\frac{\partial \Psi}{\partial \mathbf{F}} - \mathbf{S} - pJ\mathbf{F}^{-T} - J(\nabla_R \cdot \boldsymbol{\xi}_J)\mathbf{F}^{-T}\right) : \dot{\mathbf{F}} + \sum_{m\in\mathbb{M}} \nabla_R \mu_m \cdot \boldsymbol{J}_m \leq 0,\end{aligned} \tag{10}$$

Following [27, 45], we assume that the only process leading to dissipation of energy is the long-range (diffusive) transport of mobile species. Consequently, we drop any dependence on the rate of change of the model variables and impose the following constitutive laws for the chemical potentials μ_m, the macro-stress $\mathbf{S}$, the micro-stresses $\boldsymbol{\xi}$, the electric field $\boldsymbol{E}$ and the fluxes $\boldsymbol{J}_m$:

$$\mu_m = \hat{\mu}_m(\boldsymbol{\Lambda}),\ \boldsymbol{\xi}_{s,J} = \hat{\boldsymbol{\xi}}_{s,J}(\boldsymbol{\Lambda}),\ \mathbf{S} = \hat{\mathbf{S}}(\boldsymbol{\Lambda}),\ \boldsymbol{E} = \hat{\boldsymbol{E}}(\boldsymbol{\Lambda}),\ \boldsymbol{J}_m = \hat{\boldsymbol{J}}_m(\boldsymbol{\Lambda}, \nabla_R \mu_m), \tag{11}$$

where $\boldsymbol{\Lambda}$ denotes the list $\boldsymbol{\Lambda} = \{C_m, \boldsymbol{F}, \boldsymbol{H}, \nabla_R C_s, \nabla_R J\}$.

Based on Eqs. (11), the inequality (10) is linear in $\nabla_R \dot{C}_s$, $\dot{C}_m$, $\nabla_R \dot{J}$, $\dot{\boldsymbol{H}}$, $\dot{\mathbf{F}}$. Using the classical Coleman-Noll argument [48], inequality (10) must be valid for any arbitrary choice of the independent variables $\nabla_R \dot{C}_s$, $\dot{C}_m$, $\nabla_R \dot{J}$, $\dot{\boldsymbol{H}}$, $\dot{\mathbf{F}}$, so that their coefficients must be identically zero. These thermodynamic restrictions determine the specific form of the functions $\hat{\mu}_m$, $\hat{\boldsymbol{\xi}}_{s,J}$, $\hat{\mathbf{S}}$ and $\hat{\boldsymbol{E}}$ which are explicitly given by

$$\hat{\boldsymbol{\xi}}_J = \frac{\partial \Psi}{\partial \nabla_R J}, \quad \hat{\boldsymbol{\xi}}_s = \frac{\partial \Psi}{\partial \nabla_R C_s}, \quad \hat{\mu}_s = \frac{\partial \Psi}{\partial C_s} - \nabla_R \cdot \boldsymbol{\xi}_s + \nu_s p, \quad \hat{\mu}_i = \frac{\partial \Psi}{\partial C_i} + e\Phi z_i + \nu_i p, \tag{12a}$$

$$\hat{\boldsymbol{E}} = \frac{\partial \Psi}{\partial \boldsymbol{H}}, \quad \hat{\mathbf{S}} = \frac{\partial \Psi}{\partial \mathbf{F}} - pJ\mathbf{F}^{-T} + J(\nabla_R \cdot \boldsymbol{\xi}_J)\mathbf{F}^{-T} \tag{12b}$$

The energy imbalance inequality (10) then reduces to:

$$\sum_{m\in\mathbb{M}} \nabla_R \mu_m \cdot \boldsymbol{J}_m \leq 0. \tag{13}$$

We consider the system to be close to equilibrium and assume linear relationships between the fluxes $\boldsymbol{J}_m$ and the gradient terms $\nabla_R \mu_m$ so that

$$\boldsymbol{J}_m = -\sum_{\beta \in \mathbb{M}} \mathbf{M}_{\beta m} \nabla_R \mu_\beta. \tag{14}$$

To define the mobility tensors $\mathbf{M}_{\beta m}$, we adopt the Stefan–Maxwell approach [28, 29] for describing multi-component diffusive transport, which correctly captures the hydrodynamic drag (i.e. friction) between different components of the mixture [31, 32]. Full details of the calculation of $\mathbf{M}_{\beta m}$ along with a proof that the energy imbalance (13) is satisfied are provided in Appendix A.1. In summary, the diffusive fluxes are given by

$$\boldsymbol{J}_s = -\frac{C_s K}{\nu_s} \mathbf{C}^{-1} \left(\nabla_R \mu_s + \sum_{i \in \mathbb{I}} \frac{D_i}{D_i^0} \frac{C_i}{C_s} \nabla_R \mu_i \right), \tag{15a}$$

$$\boldsymbol{J}_i = -\frac{D_i C_i}{k_B T} \mathbf{C}^{-1} \nabla_R \mu_i + \frac{D_i C_i}{D_i^0 C_s} \boldsymbol{J}_s, \quad i \in \mathbb{I}, \tag{15b}$$

where $\mathbf{C} = \mathbf{F}^T \mathbf{F}$ is the right Cauchy–Green deformation tensor, and D_i and D_i^0 are the diffusivities of the i-th ionic species in the gel and in pure solvent respectively. The function K is the Darcy hydraulic permeability (over dynamic viscosity) of the gel to the solvent and ionic species, which is defined as

$$\frac{1}{K} = \frac{1}{k(J)} + \sum_{i \in \mathbb{I}} \frac{k_B T}{\nu_s D_i^0} \left(1 - \frac{D_i}{D_i^0} \right) \frac{C_i}{C_s}. \tag{16}$$

Here $k(J) = (D_s^0 / k_B T) J^\theta$ represents the Darcy hydraulic permeability (over dynamic viscosity) of the gel to pure solvent, where D_s^0 is the solvent diffusivity in the gel and θ is a parameter.

2.5. The full polyelectrolyte gel model

The governing equations for the polyelectrolyte gel are summarised and reformulated in terms of the current configuration, which provides greater physical insight into the constitutive relationships that are derived from the energy imbalance inequality. The Lagrangian form of the gel model can be found in Appendix A.2. Full details of the transformation between the reference and current states can be found in Appendix A.3. Formulating the governing equations in the current configuration also facilitates coupling the models for the gel and bath, as the bath does not have a well-defined reference configuration due to the absence of the solid phase.

Before presenting the equations describing the evolution of the gel, we introduce the model variables in the current configuration. We denote by $c_m = C_m/J$ the current concentration of mobile species, i.e., the number molecules per unit volume in $\mathcal{B}_t$. The net charge distribution is given by $q = Q/J$ with Q defined by Eq. (1f). The velocities of the mobile species $\boldsymbol{v}_m$ are related to the velocity of the network $\boldsymbol{v}_n$ via $\boldsymbol{j}_m = c_m(\boldsymbol{v}_m - \boldsymbol{v}_n)$, where $\boldsymbol{j}_m = J^{-1}\mathbf{F}\boldsymbol{J}_m$ is the diffusive flux. The Cauchy stress tensor is $\mathbf{T} = J^{-1}\mathbf{S}\mathbf{F}^T$. The electric field, the electric displacement and micro-stresses also have a counterpart in the current configuration, $\boldsymbol{e} = \mathbf{F}^{-T}\boldsymbol{E}$, $\boldsymbol{h} = J^{-1}\mathbf{F}\boldsymbol{H}$, and $\boldsymbol{\zeta}_{s,J} = J^{-1}\mathbf{F}\boldsymbol{\xi}_{s,J}$, respectively; these have been eliminated from the following sets of governing equations as $\boldsymbol{h}$ and $\boldsymbol{e}$ can be expressed in terms of $\nabla\Phi$ and the micro-stresses in terms of ∇c_s.

The full polyelectrolyte gel model in the current configuration is given by

$$J = \left(1 - \sum_m \nu_m c_m\right)^{-1}, \tag{17a}$$

$$\partial_t c_m + \nabla\cdot(c_m \boldsymbol{v}_n) = -\nabla\cdot\boldsymbol{j}_m, \;\; m \in \mathbb{M} \tag{17b}$$

$$\nabla\cdot\mathbf{T} = \mathbf{0}, \tag{17c}$$

$$-\epsilon\nabla^2\Phi = q = e\left(\sum_{i\in\mathbb{I}} z_i c_i + z_f c_f\right), \tag{17d}$$

where the network velocity satisfies $\boldsymbol{v}_n = \partial_t \boldsymbol{u} + (\boldsymbol{v}_n\cdot\nabla)\boldsymbol{u}$; the diffusive fluxes are

$$\boldsymbol{j}_s = -c_s K(c_s, c_i)\left(\nabla\mu_s + \sum_{i\in\mathbb{I}} \frac{D_i}{D_i^0}\frac{c_i}{c_s}\nabla\mu_i\right), \tag{17e}$$

$$\boldsymbol{j}_i = -\frac{D_i c_i}{k_B T}\nabla\mu_i + \frac{D_i c_i}{D_i^0 c_s}\boldsymbol{j}_s, \;\; i \in \mathbb{I}; \tag{17f}$$

and the Darcy hydraulic permeability K is defined by Eq. (16). The chemical potentials are given by

$$\mu_s = \mu_s^0 + \nu_s(p + \Pi_s) - \gamma\nabla^2 c_s, \tag{17g}$$

$$\mu_i = \mu_i^0 + \nu_i(p + \Pi_i) + z_i e\Phi, \quad i \in \mathbb{I} \tag{17h}$$

where the osmotic pressures are defined as

$$\Pi_s = \frac{k_B T}{\nu_s}\left[\frac{\chi(1-\nu_s c_s)}{J} + \ln(\nu_s c_s) + 1 - \sum_{m\in\mathbb{M}} \nu_s c_m\right], \tag{17i}$$

$$\Pi_i = \frac{k_B T}{\nu_i}\left[-\frac{\chi c_s \nu_i}{J} + \ln(\nu_i c_i) + 1 - \sum_{m\in\mathbb{M}} \nu_i c_m\right], \quad i \in \mathbb{I}. \tag{17j}$$

The stress tensor $\mathbf{T}$ can be decomposed into the sum of four terms:

$$\mathbf{T} = -p\mathbf{I} + \mathbf{T}_e + \mathbf{T}_M + \mathbf{T}_K, \tag{17k}$$

$$\mathbf{T}_M = \epsilon \left[\nabla\Phi \otimes \nabla\Phi - \frac{1}{2} |\nabla\Phi|^2 \mathbf{I} \right], \tag{17l}$$

$$\mathbf{T}_e = \frac{G}{J} \left(\mathbf{F}\mathbf{F}^T - \mathbf{I} \right), \tag{17m}$$

$$\mathbf{T}_K = \gamma \left[\left(\frac{|\nabla c_s|^2}{2} + c_s \nabla^2 c_s \right) \mathbf{I} - \nabla c_s \otimes \nabla c_s \right], \tag{17n}$$

where $\mathbf{F} = (\mathbf{I} - \nabla \boldsymbol{u})^{-1}$ is the deformation tensor, $\mathbf{T}_e$ is the elastic stress tensor, $\mathbf{T}_M$ is the Maxwell stress tensor, and $\mathbf{T}_K$ is the Korteweg stress tensor.

Compared with previous models of polyelectrolyte gels [27, 32, 36], our model is distinguished by its ability to capture the chemo-mechanical effects of internal interfaces that emerge due to phase separation. In particular, the new term $\gamma \nabla^2 c_s$ in (17g) captures the change in chemical potential across an interface and the Korteweg stress tensor $\mathbf{T}_K$ is (17k) is a bulk representation of surface tension.

3. A model for the surrounding ionic bath

In this section we present a thermodynamically consistent model for the bath that surrounds the polyelectrolyte gel. The bath model is derived following the approach developed in Section 2. However, since the bath has no solid component, the governing equations are derived directly in the current configuration, based on the standard Eulerian description commonly used in mixture theory [49]. Our detailed derivation reveals how the constraints on the mixture, such as the incompressibility and no-void conditions, are incorporated within the augmented energy imbalance inequality and alter the structure of the chemical potentials. For brevity, we present the governing equations here; full details of the derivation can be found in Appendix B.

The bath is modelled as a multi-component viscous fluid consisting of a solvent and the same N ionic species that were considered in the gel model (see Fig. 1). All species are assumed to be incompressible. We denote by c_m, $\boldsymbol{v}_m$, μ_m, and $\boldsymbol{q}_m$ the concentration, velocity, chemical potential, and diffusive flux of species $m \in \mathbb{M}$; q, Φ, $\boldsymbol{e}$, and $\boldsymbol{h}$ are the electric charge density, potential, field, and displacement; and $\mathbf{T}$ is the Cauchy stress tensor, where all of these quantities are functions of the Eulerian coordinates $\boldsymbol{x}$ and time t. Since we do not anticipate phase separation to occur in the bath, we omit the micro-stresses from the bath model.

Similar to the gel, the bath is a conductor due to the free ions, but we assume the solvent is a linear dielectric with permittivity ϵ, taken to be the same as in the gel. In the absence of the solid phase and phase separation, we drop the terms in the Helmholtz free energy associated with the elastic energy, the mixing of solvent and network and interfacial energy. Thus we have that the free energy, ψ, per unit (current) volume of the mixture, reads

$$\psi = \frac{1}{2\epsilon}\boldsymbol{h}\cdot\boldsymbol{h} + \sum_{m\in\mathbb{M}}\left[\mu_m^0 c_m + k_B T c_m \ln\left(\nu_m c_m\right)\right], \tag{18}$$

where the constants μ_m^0 are the taken to be the same as in Eq. (4). Using the free energy (18), constitutive equations for the bath can be systematically derived using an energy balance inequality.

The kinematics of the mixture are based on the volume transport approach in Brenner [50]. We thus define the volume-averaged mixture velocity as

$$\boldsymbol{v} = \sum_{m\in\mathbb{M}} \nu_m c_m \boldsymbol{v}_m. \tag{19}$$

The diffusive fluxes in the bath are defined relative to the mixture velocity as $\boldsymbol{q}_m = c_m(\boldsymbol{v}_m - \boldsymbol{v})$. We therefore obtain the following governing equations for the bath

$$\partial_t c_m + \nabla\cdot(c_m\boldsymbol{v}) = -\nabla\cdot\boldsymbol{q}_m, \quad m\in\mathbb{M}, \tag{20a}$$

$$\nabla\cdot\mathbf{T} = \mathbf{0}, \tag{20b}$$

$$-\epsilon\nabla^2\Phi = q = e\sum_{i\in\mathbb{I}} z_i c_i, \tag{20c}$$

where the fluxes are defined by

$$\boldsymbol{q}_i = -\frac{D_i^0 c_i}{k_B T}\left(\nabla\mu_i - \sum_{\beta\in\mathbb{M}}\nu_i c_\beta \nabla\mu_\beta\right) + \frac{c_i}{c_s}\boldsymbol{q}_s, \quad i\in\mathbb{I} \tag{20d}$$

$$\boldsymbol{q}_s = -\sum_{i\in\mathbb{I}}\frac{\nu_i\boldsymbol{q}_i}{\nu_s}. \tag{20e}$$

In deriving Eqs. (20d)-(20e), we have considered Stefan-Maxwell cross-diffusion as for the gel. Here the diffusion coefficients D_i^0 are defined as in Eq. (15), i.e. they indicate the diffusion coefficients of the ions in pure solvent. We assume that each point in the mixture is occupied by solvent and solute, resulting in the no-void condition

$$1 = \sum_{m\in\mathbb{M}} \nu_m c_m, \tag{20f}$$

which can be used to eliminate the solvent concentration c_s from the problem. Since we have assumed that all components of the mixture are incompressible, Eq. (20f) implies that the mixture velocity $\boldsymbol{v}$ satisfies the divergence-free condition

$$\nabla \cdot \boldsymbol{v} = 0. \tag{20g}$$

The condition $\nabla \cdot \boldsymbol{v} = 0$ is usually referred to as *quasi-incompressibility* [50] and it captures the fact that locally the volume of the mixture is conserved, in contrast to the mixture density which can change with the composition of the mixture.

The chemical potentials are given by

$$\mu_s = \mu_s^0 + \nu_s p + k_B T \left[\ln(\nu_s c_s) + 1 - \sum_{m \in \mathbb{M}} \nu_s c_m \right], \tag{20h}$$

$$\mu_i = \mu_i^0 + \nu_i p + k_B T \left[\ln(\nu_i c_i) + 1 - \sum_{m \in \mathbb{M}} \nu_i c_m \right] + z_i e \Phi, \quad i \in \mathbb{I}, \tag{20i}$$

which have contributions arising from the thermodynamic pressure p and the osmotic pressure (i.e. the terms in the parentheses). The ionic chemical potentials (20i) have an additional contribution from the electric field (i.e. the final term). The pressure dependence of the chemical potential arises from our choice to impose the no-void condition (20f) when applying the energy imbalance inequality. Imposing the divergence-free condition (20g) instead would result in functionally different, yet mathematical equivalent, forms of the chemical potentials [51].

The Cauchy stress tensor $\mathbf{T}$ can be written as

$$\mathbf{T} = -p\mathbf{I} + \mathbf{T}_M + \mathbf{T}_v, \tag{20j}$$

$$\mathbf{T}_M = \epsilon \left[\nabla\Phi \otimes \nabla\Phi - \frac{|\nabla\Phi|^2}{2}\mathbf{I} \right], \tag{20k}$$

$$\mathbf{T}_v = \eta \left(\nabla \boldsymbol{v} + \nabla \boldsymbol{v}^T \right), \tag{20l}$$

where $\mathbf{T}_M$ and $\mathbf{T}_v$ are the Maxwell and viscous stress tensor, respectively. The parameter η corresponds to the shear viscosity of the fluid, which we assume to be independent of the mixture composition. In contrast to the gel, viscous stresses need to be explicitly accounted for in the bath model. The treatment of the gel as a poroelastic medium means that viscous effects are homogenised and enter the model in the form of a Darcy-like contribution to the diffusive flux described with a permeability k.

4. Interfacial conditions

The behaviours of the polyelectrolyte gel and ionic bath are coupled via specification of interfacial boundary conditions. We denote the position of the interface in the current configuration by Γ, while $[\cdot]^+_-$ denotes the jump in the value of a variable across the interface, where $-$ and $+$ stand for the limit approaching from the gel and the bath domain respectively. The local velocity of the interface $\boldsymbol{v}_\Gamma$ is equivalent to the normal component of the network velocity $\boldsymbol{v}_n$. Thus the kinematic boundary condition reads as

$$\boldsymbol{v}_\Gamma = (\boldsymbol{v}_n \cdot \boldsymbol{n})\, \boldsymbol{n}, \tag{21a}$$

where $\boldsymbol{n} = \boldsymbol{n}(\boldsymbol{x}, t)$ is the unit normal vector to the interface. Consequently, imposing the conservation of mass across the interface and using a pillbox argument gives

$$[c_m\, (\boldsymbol{v}_m - \boldsymbol{v}_\Gamma) \cdot \boldsymbol{n}]^+_- = 0. \tag{21b}$$

Conservation of momentum leads to the continuity of the normal component of the stress tensor:

$$[\mathbf{T} \cdot \boldsymbol{n}]^+_- = \mathbf{0}. \tag{21c}$$

Assuming that there are no surface dipoles or charges on the gel-bath interface, we also have continuity of the electrical potential and the displacement field; both follow from pillbox arguments applied to Maxwell's laws:

$$[\Phi]^+_- = 0, \tag{21d}$$

$$[-\epsilon \nabla \Phi \cdot \boldsymbol{n}]^+_- = 0. \tag{21e}$$

We also impose continuity of the chemical potential:

$$[\mu_m]^+_- = 0. \tag{21f}$$

Accounting for the interfacial free energy (7) leads to the appearance of second-order derivatives in the chemical potential of solvent in the gel; see (17g). Therefore, even when the system is in equilibrium and the solvent chemical potential in the gel is a constant and equal to that of the bath, an additional boundary condition is required when solving (17g) for the solvent concentration

c_s. For simplicity, we assume that the gradient in solvent concentration vanishes at the gel-bath interface,

$$\nabla c_s|_{\Gamma^-} \cdot \boldsymbol{n} = 0, \tag{21g}$$

which implies that there is no preference for solvent molecules to accumulate or disperse at the free surface, either of which would result in a local composition gradient. Alternatively, (21g) is equivalent to imposing continuity of the (Eulerian) micro-stress $\boldsymbol{\zeta}_s$ across the interface; recall that the micro-stress in the bath is equal to zero.

Closing the model requires a slip-type boundary condition for which there exist multiple choices that are consistent with our model. For instance, Mori *et al.* [52] opted for a Navier slip condition on the solvent velocity in their kinetic model of a polyelectrolyte gel. Feng and Young [53] use a thermodynamics argument to derive a slip conditions on both the solid and solvent velocity for non-ionic gels. In Hennessy *et al.* [54], where we derive the three-dimensional electroneutral formulation of the model, we instead impose continuity of the tangential components of the mixture velocity.

The governing equations for the gel and ionic bath, together with the coupling conditions given here at the interface, are then complemented with appropriate conditions at domain boundaries. In the following section we apply the modelling framework to a one-dimensional Cartesian geometry.

5. Dynamic phase transitions and patterning of polyelectrolyte gels

In this section, we use numerical simulations to investigate the dynamic patterning of polyelectrolyte gels and how this depends on the relative sizes of the Kuhn length $L_K = \sqrt{\gamma/k_B T\nu}$ and the Debye length $L_D = \sqrt{k_B T\nu\epsilon/e^2}$, which characterise the width of the internal interfaces and electric double layers, respectively. In doing so, we specialise the model to the case of uniaxial deformations. Despite the simplified geometry, this scenario reveals the complex and wide range of behaviours that can be captured by our model, and it will serve as a useful stepping stone for understanding the dynamics that can occur in multi-dimensional settings.

In Section 5.1, we detail the reduction of the model to one dimension and discuss the electroneutral limit. In Section5.2, we look at the dynamics of volume phase transition in the regime $L_K \gg L_D$. In this case, the two length scales separate and the standard electroneutral assumption can be invoked. In Section5.3, we consider the regime in which $L_K \simeq L_D$. In this case, we

observe a novel mode patterning in the gel driven by the coupling between phase separation and the formation of electric double layers.

5.1. Geometry and model reduction

We consider a one-dimensional model of a polyelectrolyte gel that undergoes uniaxial deformations due to solvent and ion exchange with a salt bath. The gel is assumed to be bonded to an electrically insulated and impermeable substrate at $z = 0$ and have a free surface at $z = h(t)$, where we relabel the Eulerian coordinate $x_3 \equiv z$ for convenience. The deformation gradient tensor is written as $\mathbf{F} = \mathrm{diag}(1, 1, J(z,t))$. The corresponding Cauchy stress tensor has the form $\mathbf{T} = \mathrm{diag}(T_\ell(z,t), T_\ell(z,t), T(z,t))$, where T_ℓ and T capture the lateral (or transverse) and axial components of the stress, respectively. The velocity of the polymer network and the diffusive fluxes in the gel are written as $\boldsymbol{v}_n = v_n(z,t)\boldsymbol{e}_z$ and $\boldsymbol{j}_m = j_m(z,t)\boldsymbol{e}_z$, where $\boldsymbol{e}_z$ is the basis vector in the z direction. All remaining dependent variables are taken to be functions of the Eulerian coordinate z and time t, only. As discussed by Doi [55], this one-dimensional reduction corresponds to the gel being confined between two sidewalls, as shown in Figure 3; here sidewalls are either frictionless or sufficiently far apart not to influence the bulk behaviour. Many of the results presented below have been reproduced in models of cylindrical gels [54] and are expected to be generalisable to alternative geometries as well.

The bath is assumed to consist of solvent and a monovalent salt. The anionic and cationic species are denoted by subscripts $-$ and $+$, respectively; hence $z_\pm = \pm 1$. The solvent, anions, and cations, are assumed to have the same molecular volume [36] ($\nu_s = \nu_\pm \equiv \nu$). In addition, the ionic diffusivities in the gel and solution are taken to be equal, $D_\pm = D_\pm^0$. For simplicity, the bath is considered to be a large reservoir that is in equilibrium. In the far field ($z \to \infty$), the bath is assumed to be in a stress-free ($T = 0$) and electrically neutral ($c_+ = c_-$) state, and have a prescribed concentration of ions $c_\pm = c_0$. In addition, we use the far field to set the reference voltage and pressure to be zero ($\Phi = 0$ and $p = 0$).

The number of free parameters in the model is reduced by introducing the length of the gel L in the dry state and defining dimensionless variables as follows:

$$\begin{gathered} z^* = \frac{z}{L}, \quad t^* = \frac{D_s^0 t}{L^2}, \quad \phi_m = \nu c_m, \quad \mu_m^* = \frac{\mu_m - \mu_m^0}{k_B T}, \\ j_m^* = \frac{\nu L j_m}{D_s^0}, \quad v_n^* = \frac{L v_n}{D_s^0} \quad \Phi^* = \frac{e\Phi}{k_B T}, \quad \mathbf{T}^* = \frac{\mathbf{T}}{G}, \quad p^* = \frac{p}{G}. \end{gathered} \tag{22}$$

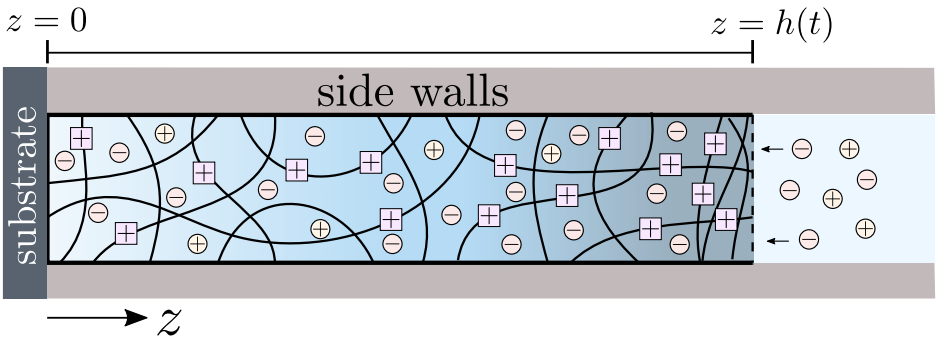

Figure 3: Sketch of a laterally confined gel swelling in a ionic bath.

The quantities ϕ_m represent volume fractions of the mobile species. In the gel, the volume fraction of polymer network can be expressed as $\phi_n = J^{-1} = 1 - \phi_s - \phi_+ - \phi_-$. Rescaling the variables according to (22) leads to the appearance of five non-dimensional parameters that are fixed for a given experimental scenario,

$$\mathcal{D}_\pm = \frac{D_\pm^0}{D_s^0}, \quad \alpha_f = z_f \nu C_f, \quad \mathcal{G} = \frac{G\nu}{k_B T}, \quad \omega = \frac{L_K}{L}, \quad \beta = \frac{L_D}{L}. \tag{23}$$

The parameters $\mathcal{D}_\pm$ are the relative diffusivities of the ions with respect to the solvent, α_f is the nominal volume fraction of fixed charges (multiplied by the valence of fixed charges), and $\mathcal{G}$ is the dimensionless shear modulus. The quantities ω and β measure, respectively, the width of diffuse internal interfaces and electric double layers relative to the typical gel dimension.

As the bath is in equilibrium, the diffusive fluxes $\boldsymbol{q}_m$ and mixture velocity $\boldsymbol{v}$ are set to zero, and the chemical potentials are constant and equal to their values in the far field. Consequently, the chemical potentials of the mobiles species are given by (upon dropping the stars for dimensionless variables)

$$\mu_s = \log \phi_s + \mathcal{G}p = \log(1 - 2\phi_0), \tag{24a}$$

$$\mu_\pm = \log \phi_\pm + \mathcal{G}p \pm \Phi = \log \phi_0. \tag{24b}$$

The second set of equalities in Eqs. (24) arises from matching to the far field as $z \to \infty$. The quantity $\phi_0 = \nu c_0$ is the salt fraction in the far field. The axial stress in the bath is

$$T = -p + \frac{1}{2}\frac{\beta^2}{\mathcal{G}}\left(\frac{\partial \Phi}{\partial z}\right)^2. \tag{25}$$

From the axial stress balance $\partial T/\partial z = 0$, we deduce that $T(z,t) \equiv 0$, which implies that the bath pressure simply balances the Maxwell stress. Re-arranging (25) leads to an expression for the

pressure which can be substituted into (24) to obtain the volume fractions of ions. Integrating once the Poisson equation for the voltage (Eq. (20c)), we obtain an equation for the electric displacement

$$-\beta\frac{\partial\Phi}{\partial z} = \sqrt{2\log(1+2\phi_0(\cosh\Phi-1))}. \tag{26}$$

Solving (26) is not necessary as it is possible to obtain a self-contained problem for the gel, as we now describe.

The non-dimensional equations for the gel consist of evolution equations for the volume fractions of mobile species given by

$$\frac{\partial\phi_m}{\partial t} + \frac{\partial}{\partial z}\left(\phi_m v_n\right) = -\frac{\partial j_m}{\partial z}. \tag{27}$$

The velocity of the polymer network and the diffusive fluxes can be expressed as

$$v_n = -\sum_{m\in\mathbb{M}} j_m, \quad j_s = -k(J)\sum_{m\in\mathbb{M}}\phi_m\frac{\partial\mu_m}{\partial z}, \quad j_\pm = -\mathcal{D}_\pm\phi_\pm\frac{\partial\mu_\pm}{\partial z} + \frac{\phi_\pm}{\phi_s}j_s, \tag{28}$$

where $k(J) = J^\theta$ is the dimensionless permeability of the gel. The chemical potentials of the mobile species are

$$\mu_s = \log\phi_s + \chi J^{-1}(1-\phi_s) + J^{-1} + \mathcal{G}p - \omega^2\frac{\partial^2\phi_s}{\partial z^2}, \tag{29a}$$

$$\mu_\pm = \log\phi_\pm + J^{-1}(1-\chi\phi_s) + \mathcal{G}p \pm \Phi. \tag{29b}$$

The axial stress in the gel, T, is equal to a constant which must be zero in order to match the axial stress of the bath at the free surface. Thus, by setting $T(z,t) = 0$, we find that the pressure in the gel is

$$p = J - J^{-1} + \frac{1}{2}\frac{\beta^2}{\mathcal{G}}\left(\frac{\partial\Phi}{\partial z}\right)^2 + \frac{\omega^2}{\mathcal{G}}\left[\phi_s\frac{\partial^2\phi_s}{\partial z^2} - \frac{1}{2}\left(\frac{\partial\phi_s}{\partial z}\right)^2\right]. \tag{30}$$

Finally, the Poisson equation (17d), for the electric potential is given by

$$-\beta^2\frac{\partial^2\Phi}{\partial z^2} = \phi_+ - \phi_- + \frac{\alpha_f}{J}. \tag{31}$$

Closing the one-dimensional model requires specification of boundary conditions at the substrate and gel-bath interface along with initial conditions. The substrate is taken to be electrically insulated and impermeable. In addition, we assume the micro-stresses to vanish at the substrate. Therefore, the corresponding boundary conditions at the substrate are given by

$$\frac{\partial\Phi}{\partial z} = 0, \quad j_m = 0, \quad \frac{\partial\phi_s}{\partial z} = 0; \quad z = 0. \tag{32}$$

At the gel-bath interface, imposing continuity of the chemical potentials and the micro-stresses leads to

$$\mu_s = \log(1-2\phi_0), \quad \mu_\pm = \log\phi_0, \quad \frac{\partial \phi_s}{\partial z} = 0; \quad z = h(t). \tag{33}$$

Continuity of the electric potential and the electric displacement generally leads to a coupling between the gel and bath models. However, (26) provides an expression for the electric displacement in the bath. Thus, by evaluating (26) at $z = h(t)$ and using the continuity of electric potentials, a nonlinear boundary condition for the electric displacement of the gel is obtained:

$$-\beta\frac{\partial \Phi}{\partial z} = \sqrt{2\log\left(1+\phi_0(\cosh\Phi - 1)\right)}, \quad z = h(t). \tag{34}$$

An integral constraint that determines the position of the free surface $h(t)$ can be found by integrating the kinematic relation $J^{-1} = \partial X_3/\partial z$ over the length of the gel and using the boundary conditions $X_3(0,t) = 0$ and $X_3(h(t),t) = 1$, which results in

$$1 = \int_0^{h(t)} \frac{1}{J(z,t)}\,\mathrm{d}z. \tag{35}$$

The initial conditions for the gel model are taken to be homogeneous equilibrium solutions that are numerically obtained for a given salt fraction in the bath ϕ_0, following the approach outlined in Appendix C. The evolution of the system towards a new equilibrium state is initiated by a sudden change ϕ_0.

5.1.1. Parameter estimation

The non-dimensional parameters appearing in the reduced model can be estimated using the representative values of the physical parameters given in Table 1. The diffusion ratios $\mathcal{D}_\pm = D_\pm^0/D_s^0 \simeq 10$ are large, indicating that ionic diffusion is fast relative to solvent diffusion. The Debye length is $L_D \simeq 10^{-10}$ m, although this is likely to underestimate the thickness of the electric double layer by not accounting for the small volume fractions of ions. For millimetre-sized gels, the corresponding value of β is 10^{-7}. The value of ω is more difficult to estimate due to uncertainties in the Kuhn length. Wu *et al.* [43] estimate that $L_K \sim 10^{-9}$ m, which results in ω being on the order of 10^{-6}.

5.1.2. The electroneutral reduction

The smallness of the parameter $\beta = L_D/L$ suggests that the one-dimensional model (27)–(35) can be simplified by taking the electroneutral limit, which is commonly invoked in modelling

Table 1: Physical parameters used in the full model (17) and characteristic length scales of the problem.

	Meaning	**Typical value(s)**	**Source**
k_B	Boltzmann's constant	1.38×10^{-23} JK^{-1}	
T	Temperature	298 K	
e	Elementary charge	1.602×10^{-19} C	
ϵ	Absolute permittivity of bath and gel (based on water)	7×10^{-10} Fm^{-1}	
ν	Volume per molecule of mobile species	10^{-28} m^3	[36]
D_i^0	Diffusivity of mobile ions in pure solvent	10^{-9} m^2 s^{-1}	[56]
D_i	Diffusivity of mobile ions in gel	$D_i = D_i^0$	
k	Hydraulic permeability of solvent in the network	$(D_s^0/k_BT)\phi_n^{-\theta}$	
θ	Exponent in permeability law	0	[47]
D_s^0	Diffusivity of the solvent in the gel	$D_s^0 = 0.1D_i^0$	[37]
χ	Flory interaction parameter	0.1–2.5	
C_f	Concentration of fixed charges in the dry gel	$\nu C_f \sim 0.01$–0.5	
G	Shear modulus	10^4–10^5 Pa	
γ	Interface stiffness parameter	$k_BT\nu L_K^2$	[43]
L	Typical length of a gel	0.001 m	
L_K	Kuhn length	$\sim 10^{-9}$ m	[43]
L_D	Width of the electric double layer (Debye length)	$L_D = \sqrt{\epsilon k_BT\nu/e^2} \sim 10^{-10}$ m	

studies of polyelectrolyte gels. Physically, the electroneutral limit exploits the small width of the electric double layer, L_D, relative to the typical dimensions of the gel, L. Thus, taking the limit $\beta = L_D/L \to 0$ collapses the electric double layer to a region of zero thickness and results in the electric potential becoming discontinuous across the gel-bath interface.

The additional length scale L_K in the phase-field model leads to multiple ways in which the electroneutral limit can be taken. If the Kuhn length L_K and the Debye length L_D are commensurate, then the internal interfaces created by phase separation are sufficiently thin to trigger the formation of electric double layers. In this case, taking the electroneutral limit would result in voltage discontinuities within the gel that must be explicitly tracked by introducing moving boundaries. However, if the Kuhn length is much larger than the Debye length, $L_K \gg L_D$, then phase separation does not trigger the formation of internal electric double layers. In this case, the electroneutral limit leads to a model for an electrically neutral gel with a smoothly varying voltage across internal interfaces.

A detailed asymptotic analysis of the full three-dimensional gel-bath model [54] revealed that all previous modelling studies which invoke the electroneutral limit implicitly assume that $L_D \ll L_K$. Although the estimates of the Debye and Kuhn lengths in Sec. 5.1.1 cast doubt on the validity of this assumption, it remains useful when taking the electroneutral limit, as the resulting model offers significant computational advantages compared to the case when $L_D \simeq L_K$. Thus, we will utilise the electroneutral model in the limit $L_D \ll L_K$ when studying the volume phase transition, which can be obtained from (27)–(35) by setting the left-hand side of (31) to zero, neglecting the $O(\beta^2)$ contributions from the Maxwell stress in the pressure (30), and replacing the boundary condition (34) with

$$\Phi = \frac{1}{2}\log\left(\frac{\phi_-}{\phi_+}\right), \quad z = h(t). \tag{36}$$

Full details can be found in Hennessy *et al.* [54].

5.2. The dynamics of the volume phase transition in electroneutral gels

The one-dimensional electroneutral model described in Sec. 5.1.2 for the case $L_D \ll L_K$ is used to explore the dynamics of the volume phase transition. The resulting equations are numerically solved using the transformation $Z = z/h(t)$ to fix the domain, finite elements for the spatial discretisation, and a semi-implicit time-stepping method for advancing the equations in time. The code has been implemented using the open-source computing platform FEniCS [57].

We first consider the volume phase transition discussed by Yu *et al.* [36], who observe good agreement between their free-swelling equilibrium solutions and the experiments by Ohmine and Tanaka [58]. In particular, their theory captures the parameter values for which a phase transition occurs. These are, in our notation, $0.7 < \chi < 1.55$, $\mathcal{G} = 1.09\times10^{-3}$, $0.02 < \alpha_f < 0.1$, $0 < \phi_0 < 0.06$. Therefore, we fix $\chi = 0.95$, $\mathcal{G} = 10^{-4}$, and $\alpha_f = 0.1$ in the model. Our non-dimensional shear modulus $\mathcal{G}$ is smaller than the reported value to compensate for the shift in the location of the volume phase transition in constrained swelling scenarios. Numerical continuation is then used to track the evolution of the homogeneous equilibria with ϕ_0 and to locate where the volume phase transition occurs. For this set of parameters, the equilibria trace out an 'S'-shaped curve that contains an interval where three solutions simultaneously exist for a given value of ϕ_0; see Figure 4 (a). The two solutions corresponding to the largest and smallest values of ϕ_s are stable [59]; hence, the system exhibits a window of bistability. In the dynamic simulations, we choose the initial state to be on the right of the bistable region by setting $\phi_0 = 0.01$. Then, at time $t = 0^+$, the ion concentration in the bath is suddenly decreased to $\phi_0 = 0.0032$ so as to drive the gel to the swollen state just to the left of the bistable region (see orange square labelled $t \gg 1$), which induces a volume phase transition.

By tracking the evolution of the gel composition, our model reveals that the phase transition occurs via the formation of a swelling front that nucleates at the free surface of the gel and propagates into the bulk; see Figures 4 (d)–(f). The onset of the phase transition when $t \simeq 750$ coincides with a marked increase in the rate of expansion of the gel and divides the evolution of the gel thickness $h(t)$ into two distinct regimes, as shown in Figure 4 (b). Horkay [26] experimentally observed the same phenomena when measuring the radius of spherical polyelectrolyte gels during their volume phase transition. The insights from our model can explain the physical origin of these distinct regimes of swelling dynamics. In the first swelling regime, before the volume phase transition sets in ($t < 750$), the influx of solvent is driven by the difference in the solvent chemical potential at the free surface and the substrate, which gives rise to smooth μ_s gradients in the gel. As time increases, the difference diminishes and the gel settles into a quasi-equilibrium state with an approximately homogeneous composition; see Figure 4 (d). The onset of the phase transition ($t \simeq 750$) rapidly divides the gel into two layers that are separated by the swelling front. The solvent chemical potential in the weakly swollen layer adjacent to the substrate quickly converges

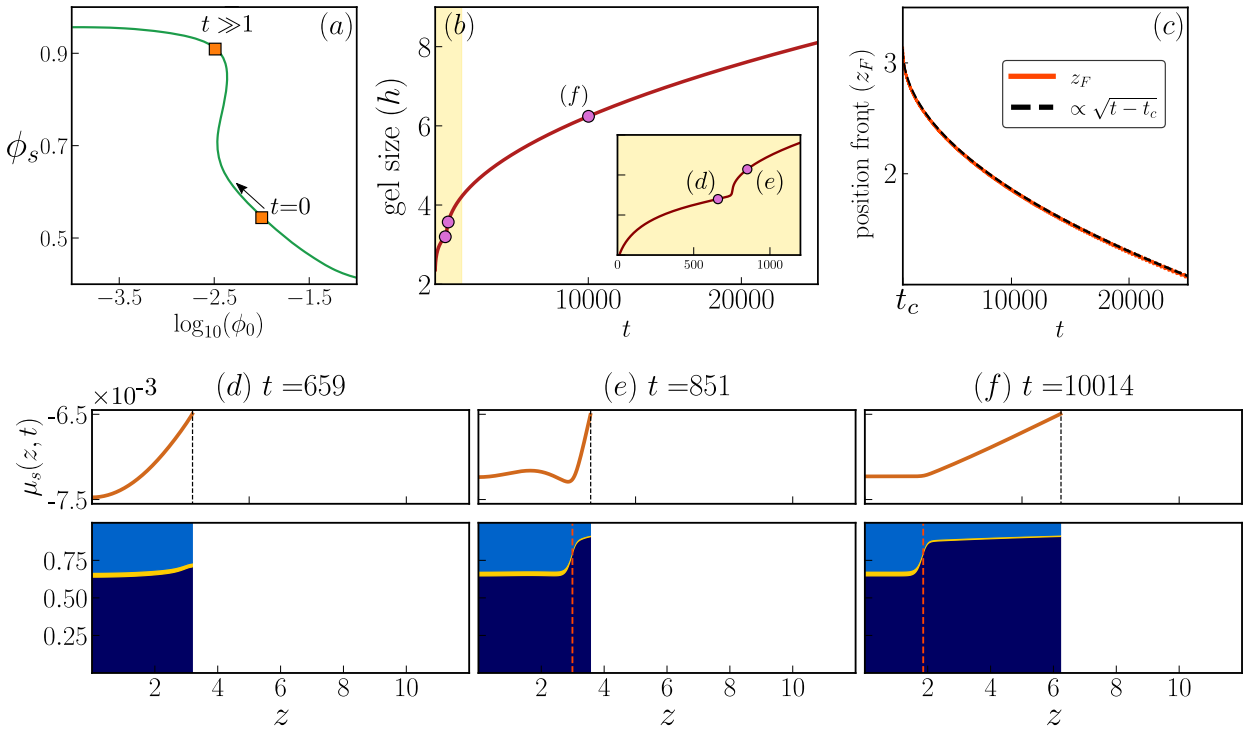

Figure 4: The volume phase transition in a swelling polyelectrolyte gel triggered by decreasing the salt fraction in the bath ϕ_0. The parameter values are $\mathcal{G} = 10^{-4}$, $\chi = 0.95$, and $\alpha_f = 0.1$. (a) The equilibrium solvent fraction in the gel ϕ_s as a function of ϕ_0. We highlight the initial and final values of ϕ_s as orange squares. (b) Evolution of the size of the gel; the pink dots indicate the time points at which the snapshots (d)–(f) are taken. (c) Evolution of the location of the front swelling front z_F, where z_F is implicitly defined as $\phi_s(z_F(t), t) = 0.8$. We find that $z_F(0) - z_F \propto \sqrt{t - t_c}$ (see comparison with black dotted line). (d)–(f) Snapshots of the solvent chemical potential μ_s and the gel composition showing volume fractions of solvent ϕ_s (dark blue), network ϕ_n (light blue), and free ions $\phi_+ + \phi_-$ (yellow). The vertical orange line indicates the location of the front z_F.

to a constant and uniform value, shown in Figures 4 (e)–(f). A gradient in the solvent chemical potential consequently develops in the highly swollen layer to ensure continuity across the swelling front and the free surface. This gradient, in turn, drives the system away from equilibrium and is responsible for the second swelling regime.

In the second swelling regime, the expansion of the gel and the propagation of the swelling front is sustained by the difference in solvent chemical potential between the free surface and the swelling front. The precise value of the chemical potential at the swelling front is determined from a Maxwell condition that captures the complex interplay between electrochemical and mechanical effects in the gel [59]. However, the position of the swelling front $z_F(t)$ retains a diffusive scaling law $z_F(0) - z_F(t) \propto \sqrt{t - t_c}$ predicted for non-ionic gels by Doi [55], where t_c denotes the time at which the phase transition occurs; see Figure 4 (c). Thus, while the electric interactions between charged species influence the properties of the Maxwell point, evidently they do not play a major role in controlling the kinetics of front propagation. Experimentally measuring the time evolution of swelling fronts would provide an ideal opportunity to quantitatively validate the model along with these hypotheses.

The model also provides a means of investigating how polyelectrolyte gels collapse (or deswell) during the volume phase transition. To study the dynamics of collapse, we keep the parameter values fixed at $\chi = 0.95$, $\mathcal{G} = 10^{-4}$, and $\alpha_f = 0.1$. The equilibria are therefore the same as those shown in Figure 4 (a). However, we now assume that the gel is initially in equilibrium with a bath that has a salt fraction of $\phi_0 = 0.0032$, which lies to the left of the region of bistability. The volume phase transition is then triggered by increasing the salt content of the bath to a value of ϕ_0 that lies to the right of the bistable region; see Figure 5 (a).

Our dynamic simulations show that, in contrast to the swelling case, the collapse of a gel can occur via two distinct routes. The first route to collapse occurs when the salt fraction in the bath is increased to $\phi_0 = 0.0042$. In this case, the collapse dynamics are analogous to the swelling dynamics illustrated in Figure 4. In particular, the volume phase transition occurs through the formation of a deswelling front that invades the gel; see Figure 5 (c)–(f). The emergence of the front also leads to two distinct deswelling regimes that can be identified in the evolution of the gel size $h(t)$, as seen in Figure 5 (b). When the salt fraction is increased from $\phi_0 = 0.0032$ to $\phi_0 = 0.01$, the second route to collapse occurs, which is distinguished by the onset of spinodal

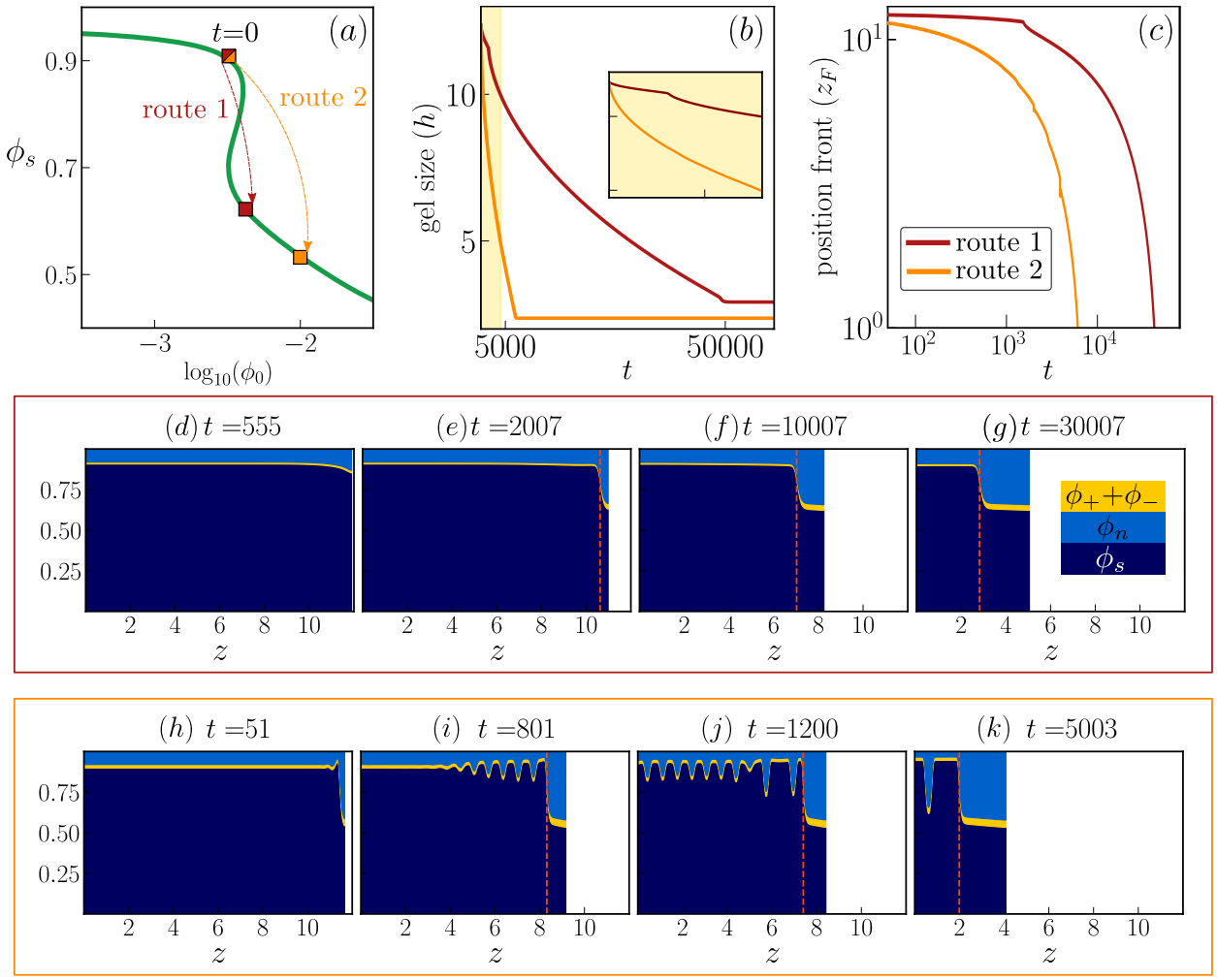

Figure 5: The two routes to gel collapse. The volume phase transition is induced by increasing the salt fraction in the bath ϕ_0. The parameter values are $\mathcal{G} = 10^{-4}$, $\chi = 0.95$, and $\alpha_f = 0.1$. The gel is initially in equilibrium with a bath with $\phi_0 = 0.0032$. At time $t = 0$, ϕ_0 is decreased to $\phi_0 = 0.0042$ (route 1) or $\phi_0 = 0.01$ (route 2). (a) The equilibrium solvent fraction in the gel ϕ_s as a function of ϕ_0. We highlight the initial and final gel solvent fractions as squares. (b) Evolution of the size of the gel $h(t)$. (c) Evolution of the location of the depletion front $z_F(t)$ defined by $\phi_s(z_F(t), t) = 0.8$. For the scenario "route 2", where multiple interfaces are presents, we denote by front the right-most interface. We use here a logarithmic scale in time to show the non-monotonic behaviour of the orange curve. (d)–(g): Snapshots of the gel composition during "route 1" of collapse. (h)–(k): Snapshots of the gel composition during "route 2" of collapse. The vertical orange line indicated the location of the front z_F.

decomposition in the bulk of the gel during front propagation; see Figure 5 (h)–(k). The new phases that spontaneously emerge within the gel continually coarsen until the front has invaded the entirety of the gel and the phase transition is complete. During the second route to collapse, the decrease in the gel size $h(t)$ is smooth (see Figure 5 (b)) and it is not possible to identify the point at which front formation is initiated. However, the evolution of the deswelling front $z_F(t)$ is more erratic in the second route compared to the first (see Figure 5 (c)) because of the interactions between the front and the localised collapsed phases that have formed within the gel.

We have investigated the rationale behind the two routes to collapse by carrying out a detailed linear stability analysis of the one-dimensional electroneutral model and constructing the associated phase diagrams in [59]. In summary, we find that, during the first route to collapse, the system initially settles into a configuration set by the Maxwell point, which lies outside of the (unstable) spinodal region of the phase diagram. The two regions that form within the gel during the volume phase transition, namely the weakly swollen region adjacent to the substrate and the highly swollen region adjacent to the free surface, are therefore stable against compositional fluctuations. During the second route to collapse, the increase in salt concentration in the bath is sufficient to drive the system into the spinodal region, which initiates phase separation within the bulk of the gel.

Experimental studies often report that morphological changes occur during gel collapse, resulting in, for example, peristaltic patterns in cylindrical gels or blisters on the gel surface [9, 60, 61]. The occurrence of spinodal decomposition during collapse provides a mechanism for morphological change by driving the gel towards a state of non-uniform stress. For the one-dimensional scenarios considered here, the only non-trivial components of stress are the lateral (transverse) stresses, which can be expressed in non-dimensional form as

$$T_\ell(t,z) = -\left(J - \frac{1}{J}\right) + \frac{\omega^2}{\mathcal{G}}\left(\frac{\partial \phi_s}{\partial z}\right)^2. \tag{37}$$

The two terms on the right-hand side of (37) represent the contributions from the elastic and Korteweg stresses, respectively. The Maxwell stresses have been neglected as they become vanishingly small in the electroneutral limit ($\beta \to 0$). The elastic component of the stress arises from the lateral confinement of the gel and is always compressive because the gel exists only in a swollen state ($J > 1$). The contribution from the Korteweg stress is always tensile and thus acts as a stabilising mechanism against elastic instability.

Using the simulation results shown in Figure 5 (h)–(k), we can track the spatio-temporal

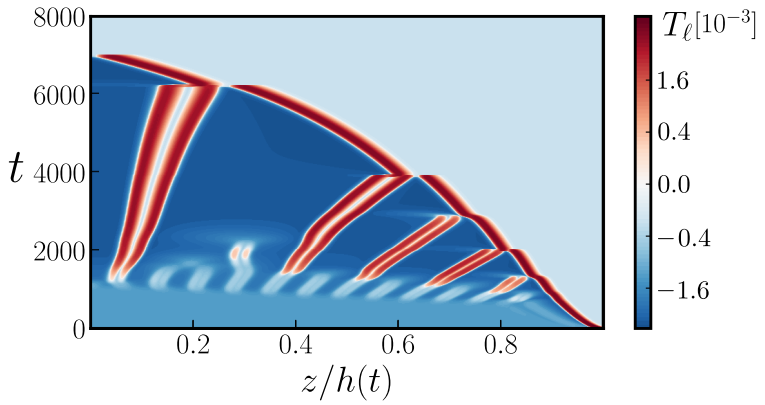

Figure 6: Time evolution and spatial distribution of the lateral stresses T_ℓ during "route 2" of the volume phase transition. The stress T_ℓ has been computed using (37) with the results of the simulations shown in Figure 5 (h)–(k).

evolution of the lateral stress during gel collapse. The initiation of spinodal decomposition has a three-fold impact on the stress distribution within the gel. Firstly, it leads to an overall increase in the compressive stress experienced by the bulk of the gel (Figure 6). This is due to the bulk of the gel tending towards a state of larger solvent content; see Figure 5 (h)–(k). Secondly, spinodal decomposition locally relaxes the compression of the gel at isolated regions that are depleted of solvent. Thirdly, the formation of thin diffuse interfaces between solvent-rich and solvent-poor phases lead to large tensile stresses where the Korteweg stress dominates the compressive elastic stress. As the internal structure of the gel changes due to thermodynamic coarsening, the stress profile evolves as well, and eventually the gel settles into a homogeneous state of compression that is reduced relative to the initial configuration.

The tensile stresses that arise in diffuse interfaces are equivalent to surface tensions that occur at sharp interfaces and are likely to play a strong role in pattern formation in higher-dimensional settings. For instance, Barrière *et al.* [62] explained the peristaltic patterns that occur during the collapse of cylindrical gels as originating from a dense skin that forms at the gel surface which is under tension. By modelling the dense skin as a surface tension at the free surface of the cylinder, they were able to qualitatively reproduce the patterns observed experimentally by Matsuo and Tanaka [9]. In the context of our one-dimensional simulations, the dense skin discussed by Barrière *et al.* can be associated with the deswollen layer that forms upstream of the propagating deswelling front; see Figure 5 (h)–(k). In our case, the deswollen layer remains under compression; however, the diffuse interface at the deswelling front naturally gives rise to the tensile

stress thought to be responsible for surface patterning. It is particularly interesting that Matsuo and Tanaka attributed the various surface patterns seen in their experiments to phase separation in the bulk of the gel, an explanation that has mainly been superseded by the capillary-driven instability proposed by Barrière *et al.* Our numerical simulations, however, indicate that phase separation and skin formation can occur simultaneously and thus suggest there is still more to be learnt about the origin of surface patterns during gel collapse.

Altering the parameter values leads to qualitatively similar modes of pattern formation in the gel. However, the bulk response of the gel, as characterised by the evolution of its thickness $h(t)$, can exhibit non-monotonic kinetics that differ from those observed in Figures 4 and 5. Motivated by the study of Wu *et al.* [20], we consider a gel with parameter values $\mathcal{G} = 10^{-3}$, $\chi = 1.75$, and $\alpha_f = 0.25$ that is initially in equilibrium with a bath that has a salt fraction of $\phi_0 = 10^{-4}$. The volume phase transition is then triggered by increasing ϕ_0 and χ to $\phi_0 = 0.05$ and $\chi = 2.4$, which leads to front propagation and spinodal decomposition; see Figure 7 (a)–(c). In this case, the gel undergoes a temporary period of swelling before ultimately shrinking and tending towards the solvent-poor collapsed state, as shown in Figure 7 (d). This non-monotonic behaviour results from the fast diffusion of ions into the gel relative to solvent diffusion. On short time scales, there is a rapid influx of cations while the total solvent content remains constant, leading to an increase in gel volume. However, on longer time scales, solvent is ejected from the gel leading to its collapse. Zhang *et al.* [32] also observed a non-monotonic evolution of the gel size in their numerical simulations. However, these authors attribute this phenomenon to Stefan–Maxwell cross-diffusion rather than the large separation of diffusive time scales between mobile species.

The onset of phase separation is responsible for the formation of non-trivial heterogeneous electronic structures within the gel. By taking the nominal volume fraction of fixed charges, α_f, to be positive, we are implicitly assuming the gel is cationic. From electroneutrality considerations, it is natural to expect that the largest concentrations of cations are found in the most swollen phases, as the high solvent content effectively dilutes the positive charges on the polyelectrolyte chains. However, this is not the case; the highest concentration of cations are found in the diffuse interfaces that form between the swollen and collapsed phases, as seen in Figure 7 (a)–(c). The origin of the high interfacial cation concentration can be traced to the Korteweg stress (recall there are no Maxwell stresses in the electroneutral limit). At the edge of the swollen phases,

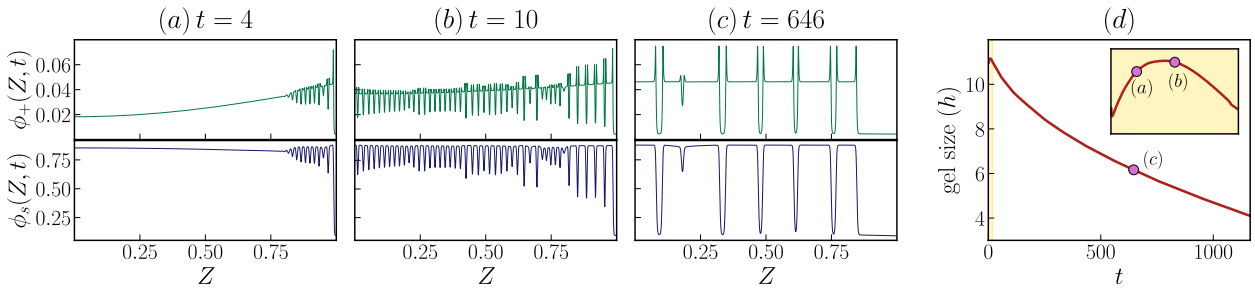

Figure 7: Spinodal decomposition in the bulk of the gel leads to a non-trivial distribution of ions, with cations becoming most concentrated at internal interfaces. (a)–(c): The volume fractions of cations ϕ_+ and solvent ϕ_s. (d): The size of the gel $h(t)$. Labels denote the time of the snapshots shown in panels (a)–(c). The parameters are set to $\mathcal{G} = 10^{-3}$, $\alpha_f = 0.25$. The gel is initially in equilibrium with the bath with salt fraction $\phi_0 = 10^{-4}$ and $\chi = 1.75$ ($\phi_s(Z,0) \equiv 0.8622$ and $\phi_+(Z,0) \equiv 4.92 \times 10^{-4}$). At time $t = 0^+$, ϕ_0 is increased to 0.05 and χ is increased to 2.4. The spatial variable Z is defined as $Z = z/h(t)$.

where $\partial^2\phi_s/\partial z^2 < 0$, the Korteweg stress is very negative. To ensure a constant value of the chemical potential, the cationic osmotic pressure, $\Pi_+ \sim \log\phi_+$, must increase to counteract the negative Korteweg stress, which in turn drives an increases the volume fraction of cations. Thus, the electronic structure within the gel is tightly coupled to the mechanical stresses that arise from phase separation.

5.3. Emergence of localised patterns from the electric double layer

In this section, we depart from the electroneutral assumption to investigate the role of the electric double layer in pattern formation within the gel. To facilitate resolving the electric double layer, we focus on the dynamics that occur in a thin region near the gel-bath interface by taking the length of the gel to be $L = 10^3 L_D$, leading to $\beta = 10^{-3}$.

5.3.1. Computation and continuation of equilibria

The electric double layer naturally leads to inhomogeneous gel configurations that persist even when equilibrium with the surrounding bath is established. We use numerical continuation to track how the non-homogeneous equilibrium states of the one-dimensional model (27)–(35) evolve as the salt fraction in the bath ϕ_0 varies. The governing equations are discretised using finite differences and the `BifurcationKit` [63] in `Julia` is employed for the continuation.

We find that the structure of the electric double layer, and hence the structure of the gel, is crucially dependent on the relative size of the Kunh length to the Debye length, the values of

which are encoded in the dimensionless parameters ω and β. In the case when $\beta \ll \omega$ (equivalent to $L_D \ll L_K$), the equilibrium curves qualitatively resemble the predictions of the electro-neutral theory. In particular, the size of the gel, h, increases as the salt fraction in the bath ϕ_0 decreases; see Fig. 8 (a.1). Moreover, the gel is homogeneous and thus electrically neutral except in a thin layer near the free boundary $z = h$, as seen in Fig. 8 (a.2)-(a.4). As ϕ_0 decreases, the width of the electric double layer decreases. These predictions agree with the standard description of the electric double layer in the literature on polyelectrolyte gels [27, 36].

However, the equilibrium curves change dramatically when β and ω are of comparable (small) magnitude (Fig. 8 (b)). For sufficiently large values of ϕ_0, there is a unique equilibrium state for the gel characterised by a homogeneous bulk and localised thin layer near the gel-bath interface. For intermediate values of ϕ_0 ($\approx 10^{-4}$), the equilibrium curve is characterised by a multi-stability region delimited by a series of saddle-node (or fold) bifurcations that are clearly visible in Fig. 8 (b.1). Here we expect linearly stable and unstable solution to alternate in order of increasing h. As shown in Figs. 8 (b.4)-(b.6), the equilibrium solutions lying in the multi-stability region of the equilibrium curves are characterised by the coexistence of two domains in the gel: a homogeneous bulk and a patterned region characterised by alternating solvent-rich spikes and collapsed dips. As the equilibrium gel thickness h increases for a fixed value of ϕ_0, the width of the patterned domain increases until it invades the entire gel. This family of solutions then persists as we decrease ϕ_0; see Fig. 8 (b.7), which corresponds to the green dot in Fig. 8 (b.1).

For a similar range of parameter values, equilibrium nanostructures have been discussed in [43]. Here a periodic domain was considered (with no bath) and homogeneous solutions were always present in the model. Our results show that such nanoscale structures can also occur for gels in contact with an ionic bath and can be spatially localised. A similar coexistence of homogeneous and patterned domains has been observed in other physical systems [64], such as copolymeric substances and ionic liquids [65]. In these systems, a similar interplay of phase separation and electrochemistry can give rise to such exciting structures which can be investigated mathematically in the context of *homoclinic snaking*.

In Fig. 9, we characterise the equilibrium solutions corresponding to $\phi_0 = 10^{-4.5}$ (see green dots in Fig. 8). We refer to the solutions in Fig. 9 (a) and Fig. 9 (b) respectively as electroneutral and phase separated gels. In Fig. 9 (a.1), we see that the net charge, q, is non-zero in the electric

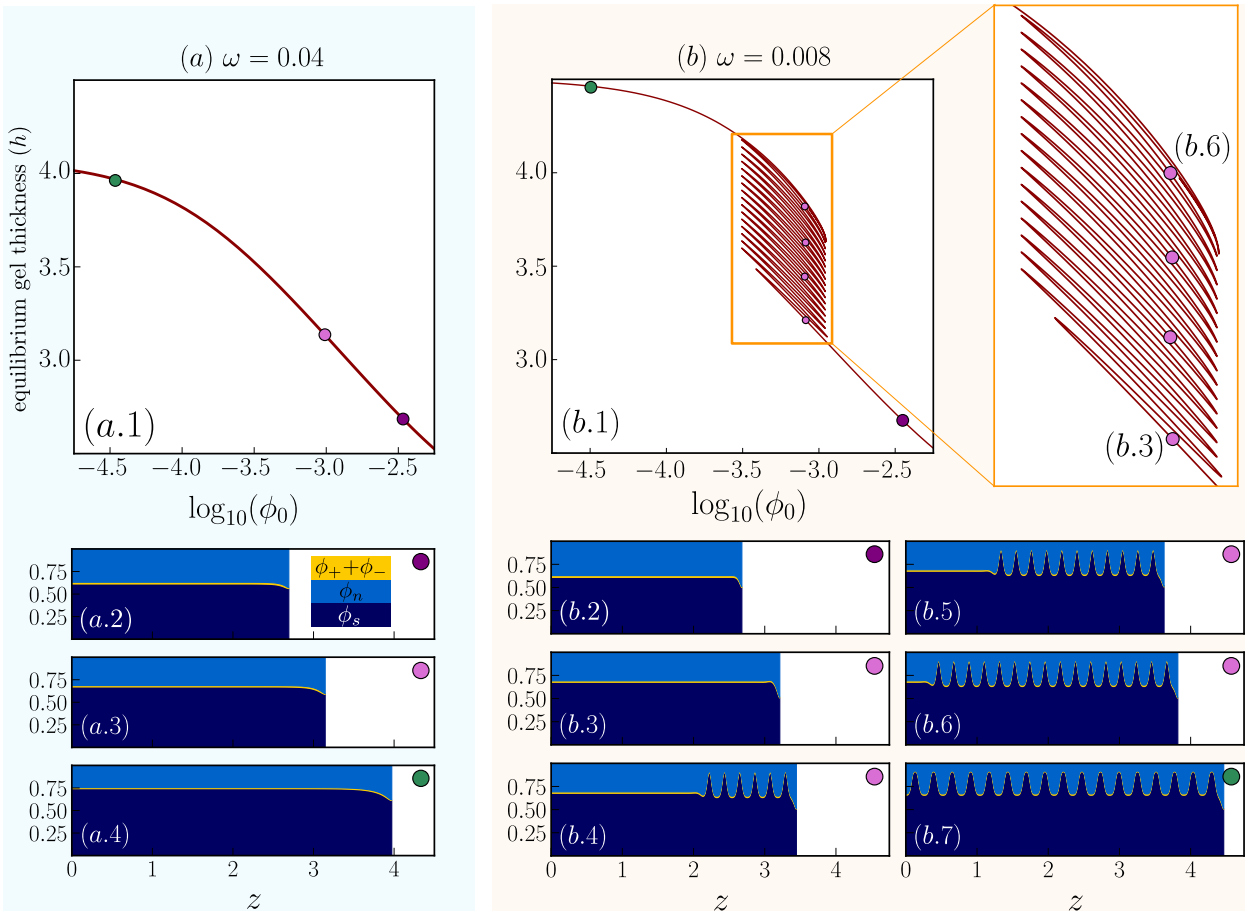

Figure 8: Non-homogeneous steady states obtained numerically by continuation for $\beta = 5 \times 10^{-3}$ and (a) much larger or (b) comparable values for ω, as stated at the top of each column. Panels in the top row for each case show the gel thickness as a function of the ion concentration ϕ_0 in the bath. The panels in the bottom row show the gel composition for several values of ϕ_0, which are identified by coloured dots: $\phi_0 = 10^{-2.45}$ (purple), $\phi_0 = 10^{-3.1}$ (magenta) and $\phi_0 = 10^{-4.45}$ (green). For the magenta dots in (b), solutions with more spikes correspond to dots with higher thickness h. The other parameters are $\mathcal{G} = 5 \times 10^{-4}$, $\chi = 0.8$ and $\alpha_f = 0.05$.

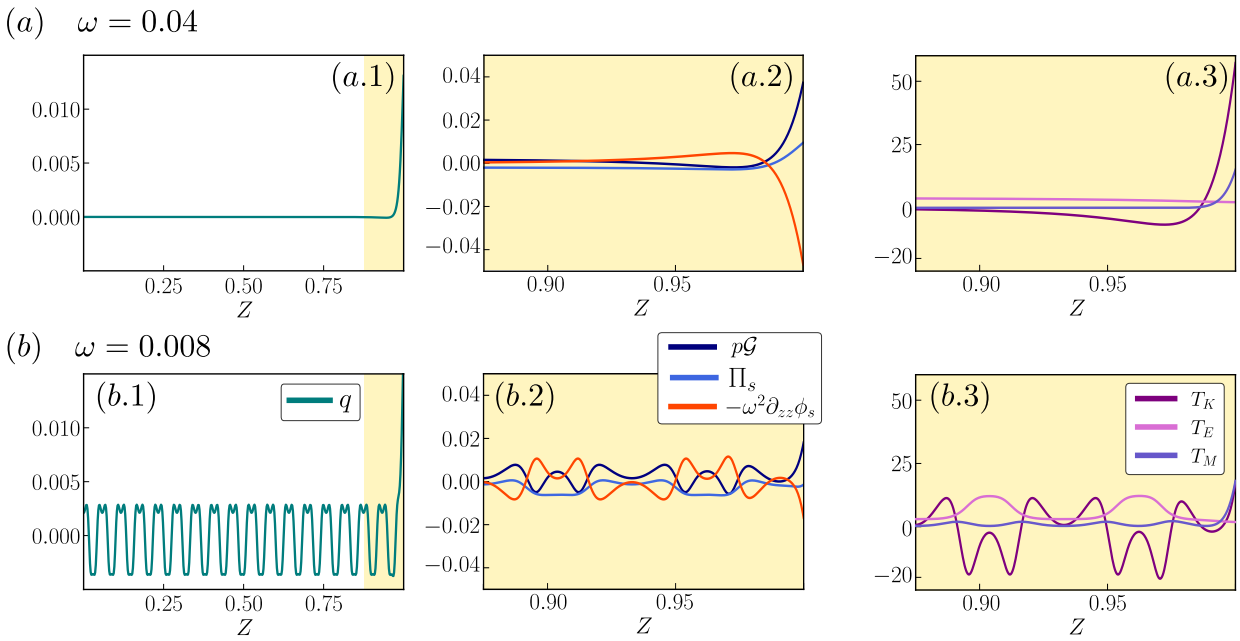

Figure 9: Characterisation of the stationary solutions with $\phi_0 = 10^{-4.45}$: (a) $\omega = 0.04$, corresponding to Fig. 8 (a.5); and (b) $\omega = 0.008$, corresponding to Fig. 8(b.8). The spatial variable is rescaled as $Z = z/h$, $Z \in [0, 1]$. In panels (a.1) and (b.1) we illustrate the charge distribution a across the gel. Away from the interface the solution either asymptotes to a constant value or to a periodic solution. We therefore focus only on the yellow area highlighted near the interface which is representative of what happens away from the free gel-bath interface. In panels (a.2) and (b.2) we illustrate the contributions to the solvent chemical potential, p is the pressure (Eq. (30)), Π_s is the osmotic pressure ($\Pi_s = \log(\phi_s) + J^{-1}(\chi(1-\phi_s)+1)$) and $-\omega^2\partial_{zz}\phi_s$ is the contribution due to the interfacial energy. In panels (a.3) and (a.4) we illustrate the spatial distribution of the axial Maxwell (T_M), Korteweg (T_K) and elastic (T_e) stresses. All other parameters are taken as in Fig. 8.

double layer while the bulk of the gel is electroneutral. In the phase separated gel, Fig. 9 (b.1), we find instead that the bulk of the gel consists of charged domains with a spatially periodic charge distribution. Integrating over the spatial domain, we find that the total charge in the electroneutral and phase separated gels are similar ($\approx 5 \times 10^{-4}$). This suggests that in the phase separated region, despite the point-wise breakdown of charge neutrality, the spatial arrangement of the charges is such that on average the bulk of the gel is electroneutral.

In Fig. 9 (a.2) and Fig. 9 (b.2), we decompose the chemical potential into its individual contribution. For the homogeneous gel (panel (a.2)), in the bulk of the gel the thermodynamic pressure (p) and the osmotic pressure, Π_s (see definition in caption Fig. 9), balances. However, near the free boundary, p and Π_s rapidly increase, and together contribute to the formation of a steep gra-

dient in the solvent volume fraction across the double layer. However, the opposing effect of the interfacial energy contribution, $-\omega^2\partial_{zz}\phi_s$, stabilises the systems and ensures the solvent volume fraction transitions smoothly across the double layer. As ω decreases, steeper gradients form in the double layer, which act as a nucleation mechanism to drive phase separation in the gel bulk, where the complex interplay between mechanics, electrostatics, and thermodynamics gives rise to periodic stable patterns.

To conclude, we focus on the axial stress distribution in the gel; see Fig. 9 (a.3) and (b.3). In the electroneutral case, the double layer is characterised by large tensile stresses, where the dominant contribution is associated to the axial Korteweg stress tensor T_K. In the phase separated gel, the tensile stresses in the double layer decrease and we find the dominant contribution is now from the Maxwell stresses T_M. As we move away from the gel-bath interface, the formation of internal interfaces and double layers result in a non trivial spatial distribution of the axial stresses whereby the dominant contribution comes from the Kortweg and elastic (T_E) stresses. The Korteweg stress T_K alternates between being negative (compressive) in the highly swollen domains (or spikes) and positive in the poorly swollen regions. The elastic stress T_E instead is always positive but is maximum in the highly swollen regions of the gel. We see that, despite the formation of internal electrical double layers, the contribution of the Maxwell stresses is negligible.

5.3.2. Dynamic simulations: transitions between equilibria

Numerically solving the time-dependent model given by (27)-(35) provides a means of exploring how the system jumps between the different stable equilibria that are observed in Fig. 8 (b.1). We use the same numerical methods as in Section 5.1 to simulate the model. The parameter values are taken to be those specified in Figure 8 (b) and we choose $\phi_0 = 10^{-3.5}$ so as to lie in the region where multiple stable equilibrium solutions are expected.

We first set the initial condition to be the equilibrum state computed for $\phi_0 = 10^{-3.5}$, corresponding to the profile like that shown in panel (b.3) of Fig. 8. We then smoothly decrease at a specific time $t_1 > 0$ the fraction in the bath ϕ_0 to a value of $10^{-4.45}$, where the gel only admits a phase separated spike-and-dip pattern that extends across the entire gel; see Fig. 8 (b). As shown in panels (c)-(d) of Fig. 10, the gel starts to phase separate by the creation of localised spikes (highly swollen regions). In contrast to spinodal decomposition, the formation of spikes is sequential and controlled, whereby each new spike appears at the boundary between the phase-separated domain

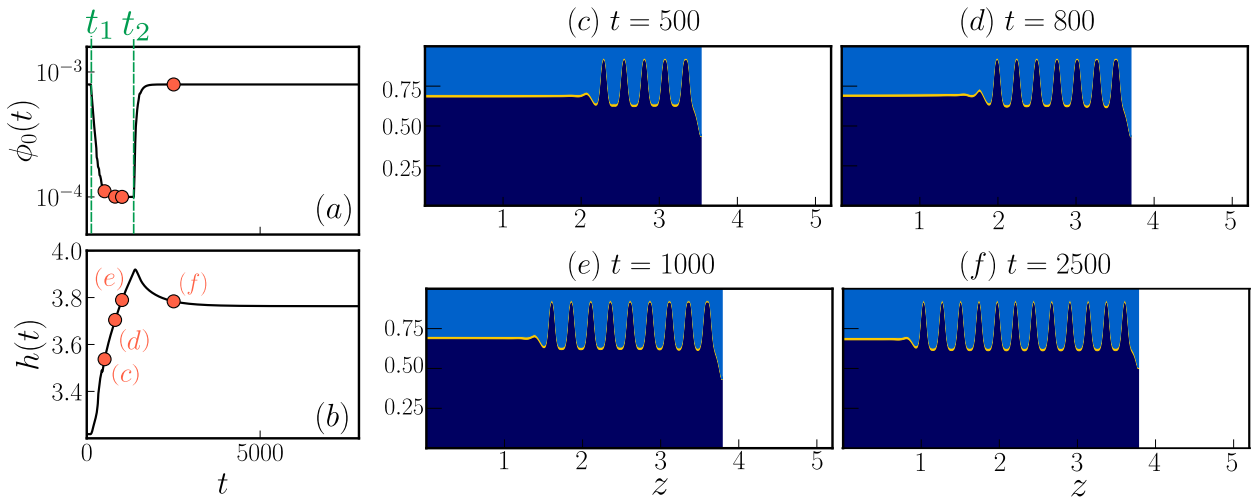

Figure 10: Numerical simulations illustrating how the interior structure of the gel can be changed by changing ϕ_0 in the bath following the procedure outlined in the main text. All other parameters are as in Fig. 8(b) with $t_1 = 100$ and $t_2 = 1350$. The final state is close to the one represented in panel (b.5) in Fig. 8.

of the gel and the inner homogeneous gel bulk. When at a time $t_2 > t_1$, the ion volume fraction in the bath ϕ_0 is increased back to its original value $\phi_0 = 10^{-3.5}$, the gel relaxes to a non-homogeneous state that differs from its initial 'electroneutral' state and has larger gel thickness; see Fig. 10 (b). Interestingly, as soon as we increase ϕ_0, no new spikes form in the gel, and those present at time $t = t_2$ are locked in. Consequently, the number of spikes in the gel at its final equilibrium state is set by the number of spikes attained by time t_2. By choosing smaller or larger values of t_2, we can therefore control the number of spikes (and hence the thickness of the gel h) that characterise the final equilibrium state of the gel. These results hint at the possibility of observing such patterned states experimentally; this can be done indirectly by measuring the size h of the gel, or directly by observing differences in the appearance of the gel close to the free boundary and further away from it. Furthermore our simulations suggest that different patterned state can be selected by appropriately choosing the conditions of the surrounding bath.

6. Conclusions and outlook

We have derived thermodynamically consistent models for a polyelectrolyte gel and the surrounding salt bath. The phase-field model of the gel is distinguished by its ability to capture the spontaneous formation and subsequent evolution of internal interfaces that appear due to phase separation. We find that the internal structure of the gel is controlled by a novel interplay between

the Debye and Kuhn lengths, L_D and L_K, which characterise the width of electric double layers and diffuse internal interfaces.

In the case of a small Debye length, $L_D \ll L_K$, the bulk of the gel remains electrically neutral, even after the onset of phase separation. However, the ions are non-uniformly distributed throughout the gel, with the cations preferentially accumulating at diffuse interfaces due to the Korteweg stress. We show that the volume phase transition occurs in electro-neutral gels via the formation of a propagating front that may be coupled to the onset of spinodal decomposition within the bulk. The formation of the front can be detected in macroscopic measurements as a sudden change in the gel size. The jump in transverse stress across the propagating front due to different degrees of swelling could also trigger a mechanical instability that manifests as detectable surface patterns. Similarly, our work confirms that phase separation can occur within the gel during its collapse, which was claimed to be the driving force behind the formation of peristaltic patterns in cylindrical gels by Matsuo and Tanaka [9]. The phase-field model presented here is well suited for use in higher-dimensional studies that explore morphological changes within polyelectrolyte gels and how these can be harnessed in emerging applications.

When the Debye and Kuhn lengths are commensurate, $L_D \simeq L_K$, we observe a new mode of self-organisation within the gel that is driven by the electric double layer at the gel-bath interface. Thus, in contrast to previous modelling studies, we find that the electric double layer plays an active and key role in the gel dynamics. The competition between the Kuhn and Debye lengths leads to the emergence of a stable, multi-layered structure in the gel with alternating positively and negatively charged phases. While electro-neutrality is locally violated at each point in the gel, it is recovered when spatially averaging over the gel volume. Mathematically, the multi-layered structure arises from the equilibrium states undergoing a cascade of bifurcations known in the literature in other contexts as *homoclinic snaking* [65]. It produces localised patterns that emanate from the electric double layer. Dynamic simulations illustrate how, by manipulating the salt fraction in the bath, it is possible to control the internal composition of the gel and drive it towards a multitude of stable configurations. Although the emerging patterns are expected to have small length scales, they can be indirectly detected from the gel size, thus providing a means to experimentally explore the results reported here. Our findings also have important consequences for the analysis and interpretation of experimental data, which is often based on fitting solutions

obtained under the assumption that the polyelectrolyte gel is homogeneous and electrically neutral. When the Kuhn and Debye lengths are similar in size, which is roughly the case according to our parameter estimates, then neither of these assumptions can be valid.

While experiments and simulations have shown rich spatio-temporal phenomena of polyelectrolyte gels, and have established their sensitivity to undergo dramatic changes in their shape and state in response to environmental variations, an in-depth understanding of the complex electrochemical and hydrodynamic interactions of various species on multiple time and spacial scales is still necessary to answer fundamental questions on the observed structural phenomena and control pattern formation. The model proposed here can open the doors to a broad range of theoretical studies to, for instance, determine whether experimentally observed structures are in equilibrium or long-lived non-equilibrium states, and which thermodynamic conditions trigger the onset of structural transitions within these complex materials.

Acknowledgments

MH recognizes support from the Mathematical Institute through a Hooke fellowship, and GC acknowledges the EPSRC and MRC Centre for Doctoral Training in Systems Approaches to Biomedical Science and Cancer Research UK for funding. All code required to generate the numerical simulations and bifurcation diagrams is available on GitHub at https://github.com/giuliacelora/KineticsPolyelectrolyteGel.

Appendix A. Model derivation for the gel

Appendix A.1. Derivation of the diffusive fluxes in the gel

Following Zhang *et al.* [32], we use a Stefan-Maxwell approach [28, 29] to describe multicomponent diffusive transport in the gel, which correctly captures the hydrodynamic drag (i.e. friction) between different components of the mixture [31]. We start from the Eulerian formulation of the reduced energy imbalance inequality (10), which we write as

$$\sum_{m\in\mathbb{M}} \nabla\mu_m \cdot \boldsymbol{j}_m \leq 0, \tag{A.1}$$

where ∇ is the spatial gradient and $\boldsymbol{j}_m$ is the diffusive flux of species m. In the current configuration, the diffusive fluxes are defined as $\boldsymbol{j}_m = c_m(\boldsymbol{v}_m - \boldsymbol{v}_n)$, where c_m and $\boldsymbol{v}_m$ are the current concentration

and velocity of species m and $\boldsymbol{v}_n$ is the velocity of the polymer network; see Appendix A.3 for more details. Inequality (A.1) can then be reformulated as

$$-\sum_{m\in\mathbb{M}} c_m \nabla\, \mu_m \cdot (\boldsymbol{v}_m - \boldsymbol{v}_n) \geq 0. \tag{A.2}$$

We assume that the system is near equilibrium and there is a linear relationship between the gradient of chemical potentials and the relative velocities $\boldsymbol{v}_m - \boldsymbol{v}_n$ so that

$$-c_m \nabla \mu_m = \sum_{\beta\in\mathbb{M}} \ell_{m\beta}(\boldsymbol{v}_\beta - \boldsymbol{v}_n), \tag{A.3}$$

where $\ell_{m\beta}$ are *phenomenological coefficients*. Given Eqs. (A.3), the inequality (A.2) can be written as [66],

$$\sum_{m\in\mathbb{M}}\sum_{\beta\in\mathbb{M}} \ell_{m\beta}(\boldsymbol{v}_\beta - \boldsymbol{v}_n)\cdot(\boldsymbol{v}_m - \boldsymbol{v}_n) \geq 0. \tag{A.4}$$

Inequality (A.4) thermodynamically constraints the coefficients $\ell_{m\beta}$ to satisfy *Onsager reciprocal relations* [67]. In the absence of magnetic effects, the matrix of phenomenological $\boldsymbol{\ell} = [\ell_{m\beta}]$ must be positive definite for A.4 to hold.

The phenomenological coefficients $\ell_{m\beta}$ can be related to drag coefficients, commonly used in mixture theory [68, 69], that can be estimated experimentally. To do so, we rewrite Eqs. (A.3) in the form

$$-c_s \nabla \mu_s = \sum_{i\in\mathbb{I}} f_{si}\,(\boldsymbol{v}_s - \boldsymbol{v}_i) + f_{sn}(\boldsymbol{v}_s - \boldsymbol{v}_n), \tag{A.5a}$$

$$-c_j \nabla \mu_j = \sum_{i\in\mathbb{I}, i\neq j} f_{ji}\,(\boldsymbol{v}_j - \boldsymbol{v}_i) + f_{js}(\boldsymbol{v}_j - \boldsymbol{v}_s) + f_{jn}(\boldsymbol{v}_j - \boldsymbol{v}_n), \quad j\in\mathbb{I}, \tag{A.5b}$$

where f_{ab} are the drag coefficients capturing the interaction between species a and b. The Onsager reciprocal relations require that $f_{mb} = f_{bm}$. A common assumption in mixture theory is that the solute-solute drag can be neglected so that $f_{ij} = 0$ for $i, j \in \mathbb{I}$ [68, 70]. The remaining drag coefficients are defined by:

$$f_{sn} = \frac{\nu_s c_s}{k}, \quad f_{js} = \frac{k_B T c_j}{D_j^0}, \quad f_{js} + f_{jn} = \frac{k_B T c_j}{D_j}, \tag{A.6}$$

where k is related to the permeability of the solvent in the network, D_j^0 is the diffusion coefficient of the solute j pure solution, and D_j is the diffusion coefficient of solute J in the gel. For this

choice of drag coefficients, the matrix $\boldsymbol{\ell}$ is:

$$\boldsymbol{\ell} = \begin{bmatrix} \mathbf{d} & -\boldsymbol{f}_s \\ -\boldsymbol{f}_s^T & d_s \end{bmatrix}, \quad \boldsymbol{f}_s = \begin{bmatrix} f_{1s} \\ \vdots \\ f_{Ns} \end{bmatrix}, \quad d_s = \sum_i f_{si} + f_{sn}. \tag{A.7}$$

Thus, $\boldsymbol{\ell}$ is a symmetric diagonally dominant matrix with positive diagonal entries and hence positive semi-definite in line with the Onsager reciprocal relations.

Using (A.5)-(A.6), along with the definition of the diffusive fluxes $\boldsymbol{j}_m = c_m(\boldsymbol{v}_m - \boldsymbol{v}_n)$, we find that

$$\boldsymbol{j}_s = -\frac{Kc_s}{\nu_s}\left(\nabla\mu_s + \sum_{i\in\mathbb{I}} \frac{D_i}{D_i^0}\frac{c_i}{c_s}\nabla\mu_i\right), \tag{A.8a}$$

$$\boldsymbol{j}_i = -\frac{D_i c_i}{k_B T}\nabla\mu_i + \frac{D_i c_i}{D_i^0 c_s}\boldsymbol{j}_s, \quad i \in \mathbb{I}, \tag{A.8b}$$

where the coefficient K is defined to be

$$\frac{1}{K} = \frac{1}{k} + \sum_{i\in\mathbb{I}} \frac{k_B T}{\nu_s D_i^0}\left(1 - \frac{D_i}{D_i^0}\right)\frac{c_i}{c_s}. \tag{A.8c}$$

Here K represents the Darcy hydraulic permeability (over dynamic viscosity) of the gel to the solvent and ionic species, whilst k represents the Darcy hydraulic permeability (over dynamic viscosity) to pure solvent. The nominal diffusive fluxes $\boldsymbol{J}_m$ can be obtained from the relation $\boldsymbol{J}_m = J\mathbf{F}^{-1}\boldsymbol{j}_m$ to produce the expressions in Eqs. (15).

Appendix A.2. Polyelectrolyte gel equations in the reference configuration

The governing equations for the gel written in terms of the reference configuration are given by

$$J = 1 + \sum_{m\in\mathbb{M}} \nu_m C_m, \tag{A.9a}$$

$$\partial_t C_s + \nabla_R \cdot \boldsymbol{J}_s = 0, \tag{A.9b}$$

$$\partial_t C_i + \nabla_R \cdot \boldsymbol{J}_i = 0, \quad i \in \mathbb{I}, \tag{A.9c}$$

$$\nabla_R \cdot \mathbf{S} = \mathbf{0}, \tag{A.9d}$$

$$\nabla_R \cdot \boldsymbol{H} = e\left(\sum_{i\in\mathbb{I}} z_i C_i + z_f C_f\right), \tag{A.9e}$$

where $\boldsymbol{H} = \epsilon J \mathbf{C}^{-1} \boldsymbol{E}$, $\boldsymbol{E} = -\nabla_R \Phi$, and $\mathbf{C} = \mathbf{F}^T \mathbf{F}$. The nominal diffusive fluxes are

$$\boldsymbol{J}_s = -K \mathbf{C}^{-1} \left(C_s \nabla_R \mu_s + \sum_i \frac{D_i}{D_i^0} C_i \nabla_R \mu_i \right), \tag{A.9f}$$

$$\boldsymbol{J}_i = -\frac{D_i}{k_B T} C_i \mathbf{C}^{-1} \nabla_R \mu_i + \frac{D_i}{D_i^0} \frac{C_i}{C_s} \boldsymbol{J}_s, \quad i \in \mathbb{I}. \tag{A.9g}$$

The micro-stresses are

$$\boldsymbol{\xi}_s = 2\gamma_1 \, \mathbf{C}^{-1} \, \nabla_R \, C_s - \gamma_3 \, \mathbf{C}^{-1} \, \nabla_R \, J, \tag{A.9h}$$

$$\boldsymbol{\xi}_J = 2\gamma_2 \, \mathbf{C}^{-1} \, \nabla_R \, J - \gamma_3 \, \mathbf{C}^{-1} \, \nabla_R \, C_s, \tag{A.9i}$$

where $\gamma_1 = \gamma/(2J)$, $\gamma_2 = \gamma C_s^2/(2J^3)$, $\gamma_3 = \gamma C_s/J^2$. The chemical potentials are written as

$$\mu_s = \mu_s^0 + \nu_s (p + \Pi_s) + \mu_s^G, \tag{A.9j}$$

$$\mu_s^G = -\nabla_R \cdot \boldsymbol{\xi}_s + G_{iJ} G_{iM} \left(\frac{\partial \gamma_1}{\partial C_s} \frac{\partial C_s}{\partial X_J} \frac{\partial C_s}{\partial X_M} + \frac{\partial \gamma_2}{\partial C_s} \frac{\partial J}{\partial X_J} \frac{\partial J}{\partial X_M} - \frac{\partial \gamma_3}{\partial C_s} \frac{\partial C_s}{\partial X_J} \frac{\partial J}{\partial X_M} \right), \tag{A.9k}$$

$$\mu_i = \mu_i^0 + \nu_i (p + \Pi_i) + z_i e \Phi, \quad i \in \mathbb{I}, \tag{A.9l}$$

where G_{iJ} are elements of the tensor $\mathbf{G} = \mathbf{F}^{-T}$ and the osmotic pressures are defined as

$$\Pi_s = \frac{k_B T}{\nu_s} \left[\ln \left(\frac{\nu_s C_s}{J} \right) + 1 - \sum_{m \in \mathbb{M}} \frac{\nu_s C_m}{J} + \frac{\chi (J - \nu_s C_s)}{J^2} \right], \tag{A.9m}$$

$$\Pi_i = \frac{k_B T}{\nu_i} \left[\ln \left(\frac{\nu_i C_i}{J} \right) + 1 - \sum_{m \in \mathbb{M}} \frac{\nu_i C_m}{J} - \frac{\chi \nu_i C_s}{J^2} \right], \quad i \in \mathbb{I}. \tag{A.9n}$$

The nominal (first Piola–Kirchhoff) stress tensor as well as the elastic and Maxwell contributions are

$$\mathbf{S} = -pJ\mathbf{F}^{-T} + \mathbf{S}_K + \mathbf{S}_M + \mathbf{S}_e, \tag{A.9o}$$

$$\mathbf{S}_e = G \left(\mathbf{F} - \mathbf{F}^{-T} \right), \tag{A.9p}$$

$$\mathbf{S}_M = -\frac{1}{\epsilon J} \left(\frac{1}{2} |\mathbf{F}\boldsymbol{H}|^2 \mathbf{I} - (\mathbf{F}\boldsymbol{H}) \otimes (\mathbf{F}\boldsymbol{H}) \right) \mathbf{F}^{-T}. \tag{A.9q}$$

Finally, the nominal Korteweg stress tensor is

$$\begin{aligned} \mathbf{S}_K \mathbf{F}^T = {} & J \frac{\partial \gamma_1}{\partial J} G_{iJ} G_{iM} \frac{\partial C_s}{\partial X_J} \frac{\partial C_s}{\partial X_M} \mathbf{I} - 2\gamma_1 (\mathbf{F}^{-T} \nabla_R C_s) \otimes (\mathbf{F}^{-T} \nabla_R C_s) \\ & - J \frac{\partial \gamma_3}{\partial J} G_{iJ} G_{iM} \frac{\partial C_s}{\partial X_J} \frac{\partial J}{\partial X_M} \mathbf{I} + 2\gamma_3 \, \mathrm{Sym}[(\mathbf{F}^{-T} \nabla_R J) \otimes (\mathbf{F}^{-T} \nabla_R C_s)] \\ & + J \frac{\partial \gamma_2}{\partial J} G_{iJ} G_{iM} \frac{\partial J}{\partial X_J} \frac{\partial J}{\partial X_M} \mathbf{I} - 2\gamma_2 (\mathbf{F}^{-T} \nabla_R J) \otimes (\mathbf{F}^{-T} \nabla_R J) - J (\nabla_R \cdot \boldsymbol{\xi}_J) \mathbf{I}, \end{aligned} \tag{A.9r}$$

where $\mathrm{Sym}[\cdot]$ denotes the symmetric part of a tensor. Note that in taking the partial derivatives of $\gamma_{1,2,3}$, we treat the variables C_s and J as independent.

Appendix A.3. Polyelectrolyte gel equations in the current configuration

To derive the equations in the current configuration, we first integrate Eqs. (1) over a reference volume $\mathcal{V}_R$ and then use the following identities to relate infinitesimal volume and surface elements in the reference and current configurations,

$$dV = JdV_R, \quad \boldsymbol{n}dS = J\mathbf{F}^{-T}\boldsymbol{N}dS_R, \tag{A.10}$$

where $\boldsymbol{N}$ and $\boldsymbol{n}$ are respectively the normal unit vector to the surface elements dS_R and dS (see Figure 2). The integral form of Eq. (1b) is given by

$$\frac{d}{dt}\int_{\mathcal{V}_R} C_m dV_R = -\int_{\mathcal{S}_R} \boldsymbol{J}_m \cdot \boldsymbol{N} dS_R, \tag{A.11}$$

which can be mapped to the current configuration using the relations (A.10), together with the Reynolds transport theorem, to give

$$\int_{\mathcal{V}(t)} \left(\frac{\partial c_m}{\partial t} + \nabla \cdot (c_m \boldsymbol{v}_n) \right) dV = -\int_{\mathcal{S}(t)} \boldsymbol{j}_m \cdot \boldsymbol{n}\, dS, \tag{A.12}$$

where $c_m = C_m/J$ is the current concentration (measured per unit volume in the current state), $\boldsymbol{j}_m = J^{-1}\mathbf{F}\boldsymbol{J}_m$ is the current flux (measured per unit area in the current state), $\boldsymbol{v}_n$ is the velocity of the polymer network, and ∇ denotes the gradient with respect to the Eulerian coordinate $\boldsymbol{x}$. Since the volume $\mathcal{V}(t)$ is arbitrary, we find that the local mass balance in Eulerian coordinates is

$$\frac{\partial c_m}{\partial t} + \nabla \cdot (c_m \boldsymbol{v}_n + \boldsymbol{j}_m) = 0, \tag{A.13}$$

where the fluxes are given by (A.8). The standard form of the species conservation law

$$\frac{\partial c_m}{\partial t} + \nabla \cdot (c_m \boldsymbol{v}_m) = 0 \tag{A.14}$$

can be recovered by defining the diffusive fluxes as $\boldsymbol{j}_m = c_m(\boldsymbol{v}_m - \boldsymbol{v}_n)$. The velocity of the polymer network $\boldsymbol{v}_n$ is linked to the solid displacement $\boldsymbol{u}$ via the relationship $\partial_t \boldsymbol{u} + (\boldsymbol{v}_n \cdot \nabla)\boldsymbol{u} = \boldsymbol{v}_n$. The displacement gradient tensor is $\mathbf{F}^{-1} = \mathbf{I} - \nabla \boldsymbol{u}$.

By applying the same procedure to remaining governing equations in Section2.2, we obtain

$$\nabla \cdot \mathbf{T} = \mathbf{0}, \tag{A.15a}$$

$$\boldsymbol{e} = -\nabla \Phi, \tag{A.15b}$$

$$\nabla \cdot \boldsymbol{h} = q, \tag{A.15c}$$

where $\mathbf{T} = J^{-1}\mathbf{S}\mathbf{F}^T = -p\mathbf{I} + \mathbf{T}_e + \mathbf{T}_M + \mathbf{T}_K$ is the Cauchy stress tensor, $\boldsymbol{e} = \mathbf{F}^{-T}\boldsymbol{E}$ is the electric field, $\boldsymbol{h} = J^{-1}\mathbf{F}\boldsymbol{H} = \epsilon\boldsymbol{e}$ is the electric displacement, and

$$q = e\left(\sum_{i\in\mathbb{I}} z_i c_i + z_f c_f\right) \tag{A.15d}$$

is the total charge density. Finally, the Eulerian formulation of the incompressibility condition Eq. (1a) is

$$J = \frac{1}{1 - \sum_{m\in\mathbb{M}} \nu_m c_m}. \tag{A.15e}$$

The expressions for the solvent chemical potential μ_s, the micro-stresses $\boldsymbol{\xi}_s$ and $\boldsymbol{\xi}_J$, and the Korteweg stress tensor $\mathbf{T}_K = J^{-1}\mathbf{S}_K\mathbf{F}^T$ are substantially simpler when written in terms of Eulerian coordinates. By using the identities

$$J\nabla_R \cdot \boldsymbol{\xi}_s = \gamma J\nabla\cdot\left(J^{-1}\nabla c_s\right) = \gamma\nabla^2 c_s - \frac{\gamma}{J^2}\nabla C_s\nabla J + \frac{\gamma C_s}{J^3}\left|\nabla J\right|^2, \tag{A.16a}$$

$$J\nabla_R \cdot \boldsymbol{\xi}_J = -\gamma J\nabla\cdot\left(\frac{c_s}{J}\nabla c_s\right) = -\gamma c_s|\nabla c_s|^2 - \gamma|\nabla c_s|^2 + \frac{\gamma C_s}{J^3}\nabla C_s\nabla J - \frac{\gamma C_s^2}{J^4}|\nabla J|^2, \tag{A.16b}$$

$$\frac{1}{2}J\gamma\nabla c_s\otimes\nabla c_s = \gamma_1\nabla C_s\otimes\nabla C_s - \gamma_3\mathrm{Sym}\left[\nabla C_s\otimes\nabla J\right] + \gamma_2\nabla J\otimes\nabla J, \tag{A.16c}$$

we find that

$$\mu_s = (p+\Pi_s)\nu_s + \mu_s^0 - \gamma\nabla^2 c_s, \tag{A.17a}$$

$$\mathbf{T}_K = \left(\gamma c_s|\nabla c_s|^2 + \frac{\gamma}{2}|\nabla c_s|^2\right)\mathbf{I} - \gamma\nabla c_s\otimes\nabla c_s, \tag{A.17b}$$

$$\boldsymbol{\xi}_s = \gamma\mathbf{F}^{-1}\nabla\, c_s, \tag{A.17c}$$

$$\boldsymbol{\xi}_J = -\gamma c_s\mathbf{F}^{-1}\nabla\, c_s. \tag{A.17d}$$

The elastic and Maxwell stress tensors can be written as

$$\mathbf{T}_e = \frac{G}{J}\left(\mathbf{B} - \mathbf{I}\right), \quad \mathbf{T}_M = \epsilon\left[\nabla\Phi\otimes\nabla\Phi - \frac{1}{2}|\nabla\Phi|^2\mathbf{I}\right], \tag{A.18}$$

where $\mathbf{B} = \mathbf{F}\mathbf{F}^T$ is the left Cauchy–Green tensor.

Appendix B. The model derivation for the bath

The derivation of the bath model begins in Appendix B.1 with a consideration of the balance laws and the equations of electrostatics in Eulerian coordinates. Then, in Appendix B.2, constitutive relations are derived using an energy imbalance inequality.

Appendix B.1. Conservation equations and electrostatics in the current configuration

We assume that each point in the mixture is occupied by solvent and/or solute, i.e. no voids can form in the mixture, resulting in the no-void condition:

$$1 = \sum_{m \in \mathbb{M}} \nu_m c_m, \tag{B.1a}$$

where c_m is the (current) concentration of species m and ν_m is its molecular volume. The concentrations c_m satisfy the balance laws

$$\frac{\partial c_m}{\partial t} + \nabla \cdot (c_m \boldsymbol{v}) = -\nabla \cdot \boldsymbol{q}_m, \quad m \in \mathbb{M}, \tag{B.1b}$$

where the volume-averaged mixture velocity $\boldsymbol{v}$ is defined as

$$\boldsymbol{v} = \sum_{m \in \mathbb{M}} \nu_m c_m \boldsymbol{v}_m, \tag{B.1c}$$

and $\boldsymbol{v}_m$ is the velocity of the m-th component of the mixture. In deriving (B.1b), we have defined the diffusive fluxes $\boldsymbol{q}_m$ relative to the mean mixture velocity $\boldsymbol{v}$ according to $\boldsymbol{q}_m = c_m(\boldsymbol{v}_m - \boldsymbol{v})$. Using the definition of mixture velocity (B.1c), together with the no-void condition (B.1a), we have that the fluxes must satisfy:

$$\sum_{m \in \mathbb{M}} \nu_m \boldsymbol{q}_m = \boldsymbol{0}. \tag{B.1d}$$

We introduce the material derivative $D(\cdot)/Dt = \partial(\cdot)/\partial t + (\boldsymbol{v} \cdot \nabla)(\cdot)$, so that equation (B.1b) takes the simple form:

$$\frac{Dc_m}{Dt} + c_m \nabla \cdot \boldsymbol{v} = -\nabla \cdot \boldsymbol{q}_m, \ m \in \mathbb{M}. \tag{B.1e}$$

By multiplying (B.1b) by ν_m, summing over m, and using (B.1a) and (B.1d), we find that the mixture velocity is divergence free:

$$\nabla \cdot \boldsymbol{v} = 0. \tag{B.1f}$$

To facilitate the derivation of state and constitutive equations for the bath, we introduce the velocity gradient tensor $\mathbf{L} = \nabla \boldsymbol{v}$. Using this notation, we can write $\nabla \cdot \boldsymbol{v} = \mathbf{I} : \mathbf{L} = \mathrm{tr}(\mathbf{L})$, where $\mathrm{tr}(\cdot)$ denotes the trace of a tensor. The tensor $\mathbf{L}$ is commonly decomposed as the sum of its symmetric ($\mathbf{D}$) and skew symmetric ($\mathbf{W}$) parts:

$$\mathbf{D} = \frac{\mathbf{L} + \mathbf{L}^T}{2}, \quad \mathbf{W} = \frac{\mathbf{L} - \mathbf{L}^T}{2}. \tag{B.2}$$

The tensor $\mathbf{D}$ is commonly called the *rate of deformation* and $\mathbf{W}$ is known as the *vorticity* or *spin* tensor.

Neglecting the inertia of the mixture (so that viscous effects dominate inertial effects corresponding to low Reynolds number of the mixture), and assuming that the bath is not subject to external forces, conservation of momentum for the mixture is:

$$\nabla \cdot \mathbf{T} = \mathbf{0}, \tag{B.3}$$

where $\mathbf{T}$ is the Cauchy stress tensor. Following [48, 71], we assume the stress tensor is symmetric, which implies balance of internal and external angular momentum; for a more detailed discussion, we refer to [71].

Finally, Maxwell's equations for the electric field $\boldsymbol{e}$, electrostatic potential Φ and the electric displacement $\boldsymbol{h}$ are analogous to those for the gel (A.15b)-(A.15c) with the charge density q given by:

$$q = \sum_{i \in \mathbb{I}} e z_i c_i. \tag{B.4}$$

Appendix B.2. The energy imbalance inequality

The energy imbalance inequality in the current configuration is

$$\frac{\mathrm{d}}{\mathrm{d}t}\left\{\int_{\mathcal{V}(t)} \psi \, dv\right\} \leq \mathcal{W}_{el}(\mathcal{V}(t)) + \int_{\mathcal{V}(t)} (\mathbf{T} : \mathbf{L}) \, dv - \sum_{m \in \mathbb{M}} \int_{\mathcal{V}(t)} \nabla \cdot (\mu_m \, \boldsymbol{q}_m) \, dv, \tag{B.5}$$

where $\mathcal{V}(t)$ is an arbitrary control volume in the bath. The terms on the right-hand side of the inequality are, in order: the rate of electrical work (specified below), the rate of mechanical work due to the stress tensor $\mathbf{T}$ and the rate at which energy is introduced in the system due to mass transport. In writing down the inequality (B.5), we have not considered any micro-stresses because we assume that phase separation does not occur in the bath. Inequality (B.5) must hold for all motions which satisfy the no-void condition (B.1a) and incompressibility condition (B.1f). However, since these two constraints are algebraically equivalent, it is sufficient to impose only one of them when using the energy imbalance inequality to derive constitutive relationships for the bath. We choose to enforce the no-void condition (B.1a) using a Lagrange multiplier λ, which allows the composition variables c_m to be treated as independent. Alternative derivations which enforce the incompressibility condition can be found in [51]. Thus, by using Reynolds' transport theorem, the

energy imbalance inequality (B.5) can be written as:

$$\int_{\mathcal{V}(t)} \left[\frac{D\psi}{Dt} + \psi \left(\mathbf{I} : \mathbf{L} \right) - \lambda \sum_m \nu_m \frac{Dc_m}{Dt} \right] dv \leq \mathcal{W}_{el}(\mathcal{V}(t)) + \int_{\mathcal{V}(t)} (\mathbf{T} : \mathbf{L})\, dv - \sum_{m \in \mathbb{M}} \int_{\mathcal{V}(t)} \nabla \cdot (\mu_m \, \boldsymbol{q}_m)\, dv. \tag{B.6}$$

To derive the rate of the electrical work in the current configuration, we start from its definition in the reference configuration (see second term on the right-hand side of Eq. (8)). We then apply the divergence theorem to obtain:

$$\mathcal{W}_{el}(\mathcal{V}(t)) = - \int_{\mathcal{V}(t)} \nabla \cdot \left(\Phi \left(\frac{D\boldsymbol{h}}{Dt} + \boldsymbol{h} \left(\mathbf{I} : \mathbf{L} \right) - \mathbf{L}\boldsymbol{h} \right) \right) dv. \tag{B.7}$$

By using (A.15b)–(A.15c), we can establish the following identities (adopting the summation convention):

$$\begin{aligned} \nabla \cdot \left(\frac{D\boldsymbol{h}}{Dt} \right) = \nabla \cdot \left(\frac{\partial \boldsymbol{h}}{\partial t} + (\boldsymbol{v} \cdot \nabla)\boldsymbol{h} \right) = \frac{\partial \nabla \cdot \boldsymbol{h}}{\partial t} + v_i \frac{\partial^2 h_j}{\partial x_i \partial x_j} \\ + \frac{\partial v_i}{\partial x_j} \frac{\partial h_j}{\partial x_i} = \frac{\partial q}{\partial t} + v_i \frac{\partial}{\partial x_i} (\nabla \cdot \boldsymbol{h}) + \nabla \boldsymbol{h}^T : \mathbf{L} = \frac{Dq}{Dt} + \nabla \boldsymbol{h}^T : \mathbf{L}, \end{aligned} \tag{B.8a}$$

$$\boldsymbol{e}\mathbf{L}\boldsymbol{h} = e_i L_{ij} h_j = e_i h_j L_{ij} = (\boldsymbol{e} \otimes \boldsymbol{h}) : \mathbf{L}, \tag{B.8b}$$

$$\nabla \cdot (\mathbf{L}\boldsymbol{h}) = \frac{\partial L_{ij}}{\partial x_i} h_j + \frac{\partial h_j}{\partial x_i} L_{ij} = \frac{\partial}{\partial x_j} \left(\frac{\partial v_i}{\partial x_i} \right) h_j + \nabla \boldsymbol{h}^T : \mathbf{L} = \nabla (\mathbf{I} : \mathbf{L}) \cdot \boldsymbol{h} + \nabla \boldsymbol{h}^T : \mathbf{L}. \tag{B.8c}$$

Thus, (B.7) reduces to:

$$\mathcal{W}_{el}(\mathcal{V}(t)) = \int_{\mathcal{V}(t)} \left(\boldsymbol{e} \frac{D\boldsymbol{h}}{Dt} + [p_{el} \mathbf{I} - \boldsymbol{e} \otimes \boldsymbol{h}] : \mathbf{L} - \Phi \frac{Dq}{Dt} \right) dv, \tag{B.9a}$$

where

$$p_{el} = (\boldsymbol{e} \cdot \boldsymbol{h}) - \Phi (\nabla \cdot \boldsymbol{h}). \tag{B.9b}$$

Using the specified form of the free energy (18) along with (B.9) enables the energy imbalance inequality (B.6) to be written as

$$\begin{aligned} (\mathbf{T}_{equi} - \mathbf{T}) : \mathbf{L} + \left(\frac{\partial \psi}{\partial \boldsymbol{h}} - \boldsymbol{e} \right) \cdot \frac{D\boldsymbol{h}}{Dt} + \sum_{i \in \mathbb{I}} \left[e z_i \Phi - \mu_i + \nu_i \lambda + \frac{\partial \psi}{\partial c_i} \right] \frac{Dc_i}{Dt} \\ + \left(\nu_s \lambda - \mu_s + \frac{\partial \psi}{\partial c_s} \right) \frac{Dc_s}{Dt} + \sum_{m \in \mathbb{M}} \nabla \mu_m \cdot \boldsymbol{q}_m \leq 0, \end{aligned} \tag{B.10}$$

where we define $\mathbf{T}_{equi}$ as

$$\mathbf{T}_{equi} = -p_{el} \mathbf{I} + \boldsymbol{e} \otimes \boldsymbol{h} + \left(\psi - \sum_{m \in \mathbb{M}} \mu_m c_m \right) \mathbf{I}. \tag{B.11}$$

Guided by the inequality (B.10), we define the following constitutive equations for the chemical potentials, the electric field, the fluxes and the stress tensor:

$$\mu_m = \hat{\mu}_m(c_m, \boldsymbol{h}), \tag{B.12a}$$

$$\boldsymbol{e} = \hat{\boldsymbol{e}}(c_m, \boldsymbol{h}), \tag{B.12b}$$

$$\mathbf{T} = \hat{\mathbf{T}}(c_m, \boldsymbol{h}, \mathbf{L}) = \mathbf{T}_{equi}(c_m, \boldsymbol{h}) + \mathbf{T}_v(c_m, \boldsymbol{h}, \mathbf{L}), \tag{B.12c}$$

$$\boldsymbol{q}_m = \hat{\boldsymbol{q}}_m(c_m, \boldsymbol{h}, \nabla\mu_m). \tag{B.12d}$$

The dependence of $\mathbf{T}_v$ on the velocity gradient $\mathbf{L}$ enables viscous dissipation to be explicitly accounted for via a viscous contribution to the stress tensor. In the gel, viscous dissipation is accounted for in the diffusive fluxes via a Darcy contribution describing pressure-driven flow. Given the form on the constitutive laws in Eqs. (B.12), the inequality (B.10) is linear in the rates $D\boldsymbol{h}/Dt$, Dc_m/Dt with $m \in \mathbb{M}$, each of which can be chosen independently at each point $\boldsymbol{x}$ and time t. For the energy imbalance inequality to be always satisfied, we must have that

$$\mu_s = \mu_s^0 + \nu_s p + k_B T \left[\ln(\nu_s c_s) + 1 - \sum_{j\in\mathbb{M}} \nu_s c_j \right], \tag{B.13a}$$

$$\mu_i = \mu_i^0 + \nu_i p + k_B T \left[\ln(\nu_i c_i) + 1 - \sum_{j\in\mathbb{M}} \nu_i c_j \right] + z_i e\Phi, \quad i \in \mathbb{I} \tag{B.13b}$$

$$\boldsymbol{e} = \epsilon^{-1}\boldsymbol{h}, \tag{B.13c}$$

$$\mathbf{T}_{equi} = -p\mathbf{I} + \epsilon^{-1}\boldsymbol{h}\otimes\boldsymbol{h} - \frac{|\boldsymbol{h}|^2}{2\epsilon}\mathbf{I}, \tag{B.13d}$$

where $\mathbf{T}_{equi}$ has been simplified using the definition of the Helmholtz free energy (18) and by introducing the thermodynamic pressure p defined as $p = \lambda + k_B T \sum_{m\in\mathbb{M}} c_m$. The energy imbalance (B.10) then reduces to:

$$-\mathbf{T}_v : \mathbf{L} + \sum_{m\in\mathbb{M}} \nabla\mu_m \cdot \boldsymbol{q}_m \leq 0. \tag{B.14}$$

Given the symmetry of the stress tensor $\mathbf{T}$ and the fact that $\mathbf{T}_{equi}$ is symmetric (as verified below), we must have that $\mathbf{T}_v$ is symmetric. We then have that $\mathbf{T} : \mathbf{W} = 0$, so that $\mathbf{L} = \mathbf{D} + \mathbf{W}$ can be substituted by $\mathbf{D}$ in (B.14). Utilising the definition of the mixture velocity (B.1c) together with the relationship $\boldsymbol{q}_m = c_m(\boldsymbol{v}_m - \boldsymbol{v})$, Eq (B.14) can be rewritten as:

$$-\mathbf{T}_v : \mathbf{D} + \sum_{m\in\mathbb{M}} c_m \left(\nabla\mu_m - \sum_{\beta\in\mathbb{M}} c_\beta \nu_m \nabla\mu_\beta \right) \cdot \boldsymbol{v}_m \leq 0. \tag{B.15}$$

Assuming that we are in the regime of linear non-equilibrium thermodynamics and considering the additional constraint imposed by *Curie's law*, *i.e.*, there cannot be any coupling between thermodynamic variables of different tensorial nature, we arrive at the following set of force-flux relations

$$\mathbf{T}_v = 2\eta\left(\mathbf{D} - \frac{1}{3}(\mathbf{I}:\mathbf{D})\mathbf{I}\right) + \kappa(\mathbf{I}:\mathbf{D})\mathbf{I}, \tag{B.16a}$$

$$-c_m\left(\nabla\mu_m - \sum_{\beta\in\mathbb{M}}\nu_m c_\beta \nabla\mu_\beta\right) = \sum_{k\in\mathbb{M}}\ell_{km}\boldsymbol{v}_k, \quad m\in\mathbb{M}, \tag{B.16b}$$

where the matrix of phenomenological coefficients $\boldsymbol{\ell} = [\ell_{ij}]$ must be symmetric and positive definite, while η and κ are positive constants representing the shear and dilatational viscosity of the bath, respectively. Note that the latter will not actually play a role as the isotropic component of $\mathbf{T}_v$ will vanish upon strongly imposing the divergence-free condition (1a).

To determine the velocities $\boldsymbol{v}_m$ and hence the diffusive fluxes $\boldsymbol{q}_m$, we assume that the transport of mobile species in the bath obeys Stefan–Maxwell diffusion [28, 29]. We can therefore relate the phenomenological coefficients ℓ_{ij} to the drag coefficients used in mixture theory. To do so, we rewrite equation (B.16b) in terms of the relative velocities between the different phases:

$$-c_m\left(\nabla\mu_m - \sum_{\beta\in\mathbb{M}}\nu_m c_\beta \nabla\mu_\beta\right) = \sum_{k\in\mathbb{M}\setminus\{m\}} f_{km}\left(\boldsymbol{v}_m - \boldsymbol{v}_k\right), \quad m\in\mathbb{M}. \tag{B.17}$$

We neglect solute-solute drag and use the expressions for $f_{si} = f_{is}$ given in (A.6). Analogously to the result in Appendix A.1, for this choice of the fluxes, we have that the matrix $\boldsymbol{\ell}$ has the same structure as in Eq. (A.7) by setting $f_{mn} = 0$ for all $m\in\mathbb{M}$. Therefore $\boldsymbol{\ell}$ is still a symmetric and diagonally dominated matrix and hence positive semi-definite.

Equation (B.17) is an underdetermined system for the velocities $\boldsymbol{v}_m$, which can be seen by summing over $m\in\mathbb{M}$ to show that both sides are identically zero. This is to be expected as the velocities are not independent but need to satisfy (B.1d). We therefore use (B.17) to express the ionic velocities in terms of $\boldsymbol{v}_s$, where the latter is defined by (B.1d). All this considered, we obtain:

$$\boldsymbol{v}_i = -\frac{D_i^0}{k_B T}\left(\nabla\mu_i - \sum_{\beta\in\mathbb{M}}\nu_i c_\beta\nabla\mu_\beta\right) + \boldsymbol{v}_s, \ i\in\mathbb{I}. \tag{B.18}$$

Simply subtracting the mixture velocity and multiplying by the ionic concentration c_i we find that

diffusive fluxes can be written as

$$\boldsymbol{q}_i = -\frac{D_i^0 c_i}{k_B T}\left(\nabla\mu_i - \sum_{\beta\in\mathbb{M}} \nu_i c_\beta \nabla\mu_\beta\right) + \frac{c_i}{c_s}\boldsymbol{q}_s, \tag{B.19a}$$

$$\boldsymbol{q}_s = -\sum_{i\in I}\frac{\nu_i}{\nu_s}\boldsymbol{q}_i, \tag{B.19b}$$

where (B.19b) is obtained by simply rearranging the terms in (B.1d).

Appendix C. Homogeneous equilibrium solutions for a constrained gel

The homogeneous steady states of (27)–(35) can be obtained by setting $\phi_m(\boldsymbol{x},t) \equiv \bar{\phi}_m$ with $m \in \{s,+,-\}$, $J(\boldsymbol{x},t) \equiv \bar{J}$, $p(\boldsymbol{x},t) \equiv \bar{p}$ and $\Phi(\boldsymbol{x},t) \equiv \bar{\Phi}$. Imposing continuity of chemical potential across the gel-bath interface leads to

$$\bar{p} = \left(\bar{J}^2 - 1\right)\bar{J}^{-1}, \tag{C.1a}$$

$$0 = \alpha_f \bar{J}^{-1} + \bar{\phi}_+ - \bar{\phi}_- \tag{C.1b}$$

$$\ln(1-2\phi_0) = \mathcal{G}\left(\bar{J}^2 - 1\right)\bar{J}^{-1} + \left[\ln(\bar{\phi}_s) + \frac{\chi(1-\bar{\phi}_s)+1}{\bar{J}}\right], \tag{C.1c}$$

$$\ln(\phi_0) = \mathcal{G}\left(\bar{J}^2 - 1\right)\bar{J}^{-1} + \bar{\Phi} + \ln(\bar{\phi}_+) - \frac{\chi\bar{\phi}_s - 1}{J}, \tag{C.1d}$$

$$\ln(\phi_0) = \mathcal{G}\left(\bar{J}^2 - 1\right)\bar{J}^{-1} - \bar{\Phi} + \ln(\bar{\phi}_-) - \frac{\chi\bar{\phi}_s - 1}{J}, \tag{C.1e}$$

$$\bar{J} = \left(1 - \bar{\phi}_s - \bar{\phi}_+ - \bar{\phi}_-\right)^{-1}. \tag{C.1f}$$

Subtracting (C.1d) from (C.1e) and (C.1c), and using (C.1b), we obtain:

$$\bar{\phi}_\pm = \mp\frac{\alpha_f\bar{J}^{-1}}{2} + \sqrt{\left(\frac{\alpha_f\bar{J}^{-1}}{2}\right)^2 + \frac{\phi_0^2\bar{\phi}_s^2}{(1-2\phi_0)^2}\exp\left(2\chi\bar{J}^{-1}\right)}, \tag{C.2a}$$

$$\bar{\Phi} = \frac{1}{2}\ln\left(\bar{\phi}_-\bar{\phi}_+^{-1}\right), \tag{C.2b}$$

Equations (C.2) are a generalisation of the standard Donnan Equilibrium [72, 73] to our specific problem, where the additional exponential contribution in (C.2a) due to the mixing energy has to be considered. Using (C.2) to simplify the system (C.1), the latter reduces to:

$$0 = \mathcal{G}\left(\bar{J}^2 - 1\right)\bar{J}^{-1} + \ln\left(\frac{\bar{\phi}_s}{1-2\phi_0}\right) + (\chi(1-\bar{\phi}_s)+1)\bar{J}^{-1}, \tag{C.3a}$$

$$0 = \bar{J}^{-1} - 1 + \bar{\phi}_s + 2\sqrt{\left(\frac{\alpha_f\bar{J}^{-1}}{2}\right)^2 + \frac{\phi_0^2\bar{\phi}_s^2}{(1-2\phi_0)^2}\exp\left(2\chi\bar{J}^{-1}\right)}, \tag{C.3b}$$

where the only two unknowns are $\bar{\phi}_s$ and $\bar{J}$. Equations (C.3) define the equilibrium curves presented in the figures in Section5.2 which can be computed using arclength continuation methods.

References

[1] T. Tanaka, Collapse of gels and the critical endpoint, Phys. Rev. Lett. 40 (1978) 820–823. doi:10.1103/PhysRevLett.40.820.

[2] A. Dobrynin, Theory and simulations of charged polymers: From solution properties to polymeric nanomaterials, Current Opinion in Colloid & Interface Science 13 (2008) 376–388. doi:10.1016/j.cocis.2008.03.006.

[3] M. S. Dimitriyev, Y.-W. Chang, P. M. Goldbart, A. Fernández-Nieves, Swelling thermodynamics and phase transitions of polymer gels, Nano Futures 3 (2019) 042001. doi:10.1088/2399-1984/ab45d5.

[4] J. L. Mccoy, M. Muthukumar, Dynamic light scattering studies of ionic and nonionic polymer gels with continuous and discontinuous volume transitions, Journal of Polymer Science Part B: Polymer Physics 48 (2010) 2193–2206. doi:10.1002/polb.22101.

[5] M. Mussel, F. Horkay, Experimental Evidence for Universal Behavior of Ion-Induced Volume Phase Transition in Sodium Polyacrylate Gels, The Journal of Physical Chemistry Letters 10 (2019) 7831–7835. doi:10.1021/acs.jpclett.9b03126.

[6] F. Horkay, I. Tasaki, P. J. Basser, Effect of monovalent-divalent cation exchange on the swelling of polyacrylate hydrogels in physiological salt solutions, Biomacromolecules 2 (2001) 195–199. doi:10.1021/bm0056153.

[7] T. Bertrand, J. Peixinho, S. Mukhopadhyay, C. W. MacMinn, Dynamics of swelling and drying in a spherical gel, Physical Review Applied 6 (2016) 064010. doi:10.1103/PhysRevApplied.6.064010.

[8] K. Dusek, D. Patterson, Transition in swollen polymer networks induced by intramolecular condensation, Journal of Polymer Science Part A-2: Polymer Physics 6 (1968) 1209–1216. doi:10.1002/pol.1968.160060701.

[9] E. S. Matsuo, T. Tanaka, Patterns in shrinking gels, Nature 358 (1992) 482–485. doi:10.1038/358482a0.

[10] A. Y. Zubarev, F. A. Blyakhman, G. H. Pollack, P. Gusev, A. P. Safronov, Self-Similar Wave of Swelling/Collapse Phase Transition along Polyelectrolyte Gel, Macromolecular Theory and Simulations 13 (2004) 697–701. doi:10.1002/mats.200400027.

[11] A. R. Khokhlov, E. Y. Kramarenko, Weakly charged polyelectrolytes: Collapse induced by extra ionization, Macromolecules 29 (1996) 681–685. doi:10.1021/ma946426d.

[12] J. Hua, M. K. Mitra, M. Muthukumar, Theory of volume transition in polyelectrolyte gels with charge regularization, The Journal of Chemical Physics 136 (2012) 134901. doi:10.1063/1.3698168.

[13] C. E. Sing, J. W. Zwanikken, M. Olvera de la Cruz, Effect of ion–ion correlations on polyelectrolyte gel collapse and reentrant swelling, Macromolecules 46 (2013) 5053–5065. doi:10.1021/ma400372p.

[14] D. Buenger, F. Topuz, J. Groll, Hydrogels in sensing applications, Progress in Polymer Science 37 (2012) 1678–1719. doi:10.1016/j.progpolymsci.2012.09.001.

[15] S. Chaterji, I. K. Kwon, K. Park, Smart polymeric gels: Redefining the limits of biomedical devices, Progress in Polymer Science 32 (2007) 1083–1122. doi:10.1016/j.progpolymsci.2007.05.018.

[16] W. Hong, Continuum models of stimuli-responsive gels, in: Advances in Soft Matter Mechanics, Springer Berlin Heidelberg, Berlin, Heidelberg, 2012, pp. 165–196. doi:10.1007/978-3-642-19373-6_6.

[17] M. A. Stuart, W. T. Huck, J. Genzer, M. Müller, C. Ober, M. Stamm, G. B. Sukhorukov, I. Szleifer, V. V. Tsukruk, M. Urban, F. Winnik, S. Zauscher, I. Luzinov, S. Minko, Emerging applications of stimuli-responsive polymer materials, Nature Materials 9 (2010) 101–113. doi:10.1038/nmat2614.

[18] T. Tanaka, S.-T. Sun, Y. Hirokawa, S. Katayama, J. Kucera, Y. Hirose, T. Amiya, Mechanical instability of gels at the phase transition, Nature 325 (1987) 796–798. doi:10.1038/325796a0.

[19] M. Shibayama, Spatial inhomogeneity and dynamic fluctuations of polymer gels, Macromolecular Chemistry and Physics 199 (1998) 1–30. doi:10.1002/(SICI)1521-3935(19980101)199:1<1::AID-MACP1>3.0.CO;2-M.

[20] K.-A. Wu, P. K. Jha, M. O. de la Cruz, Control of Nanophases in Polyelectrolyte Gels by Salt Addition, Macromolecules 43 (2010) 9160–9167. doi:10.1021/ma101726v.

[21] K. A. Rosowski, T. Sai, E. Vidal-Henriquez, D. Zwicker, R. W. Style, E. R. Dufresne, Elastic ripening and inhibition of liquid–liquid phase separation, Nature Physics 16 (2020) 422–425. doi:10.1038/s41567-019-0767-2.

[22] K. A. Rosowski, E. Vidal-Henriquez, D. Zwicker, R. W. Style, E. R. Dufresne, Elastic stresses reverse Ostwald ripening, Soft Matter 16 (2020) 5892–5897. doi:10.1039/D0SM00628A.

[23] C. P. Brangwynne, P. Tompa, R. V. Pappu, Polymer physics of intracellular phase transitions, Nature Physics 11 (2015) 899–904. doi:10.1038/nphys3532.

[24] R. W. Style, T. Sai, N. Fanelli, M. Ijavi, K. Smith-Mannschott, Q. Xu, L. A. Wilen, E. R. Dufresne, Liquid Phase Separation in an Elastic Network, Physical Review X 8 (2018) 011028. doi:10.1103/PhysRevX.8.011028.

[25] X. Wang, W. Hong, et al., Surface interactions between two like-charged polyelectrolyte gels, Physical Review E 81 (2010) 041803. doi:10.1103/PhysRevE.81.041803.

[26] F. Horkay, Polyelectrolyte gels: A unique class of soft materials, Gels 7 (2021) 102. doi:10.3390/gels7030102.

[27] W. Hong, X. Zhao, Z. Suo, Large deformation and electrochemistry of polyelectrolyte gels, Journal of the Mechanics and Physics of Solids 58 (2010) 558–577. doi:10.1016/j.jmps.2010.01.005.

[28] J. Stefan, Über Das Gleichgewicht Und Die Bewegung Insbesondere Die Diffusion Von Gasgemengen, Sitzungsber. Akad. Wiss. Wien 63(2) (1871) 63–124.

[29] J. C. Maxwell, IV. On the dynamical theory of gases, Phil. Trans. R. Soc. 157 (1867) 49–88. doi:10.1098/rstl.1867.0004.

[30] R. Krishna, J. Wesselingh, The Maxwell-Stefan approach to mass transfer, Chemical Engineering Science 52 (1997) 861 – 911. doi:10.1016/S0009-2509(96)00458-7.

[31] D. Bothe, P.-E. Druet, On the structure of continuum thermodynamical diffusion fluxes–A novel closure scheme and its relation to the Maxwell-Stefan and the Fick-Onsager approach (2020). arXiv:2008.05327.

[32] H. Zhang, M. Dehghany, Y. Hu, Kinetics of polyelectrolyte gels, Journal of Applied Mechanics 87 (2020). doi:10.1115/1.4046737.

[33] M. E. Gurtin, E. Fried, L. Anand, The Mechanics and Thermodynamics of Continua, Cambridge University Press, 2010. doi:10.1017/cbo9780511762956.

[34] A. Drozdov, Swelling of pH-responsive cationic gels: Constitutive modeling and structure–property relations, International Journal of Solids and Structures 64-65 (2015) 176 – 190. doi:10.1016/j.ijsolstr.2015.03.023.

[35] A. D. Drozdov, J. deClaville Christiansen, Modeling the effects of pH and ionic strength on swelling of anionic polyelectrolyte gels, Modelling and Simulation in Materials Science and Engineering 23 (2015) 055005. doi:10.1088/0965-0393/23/5/055005.

[36] Y. Yu, C. M. Landis, R. Huang, Salt-induced swelling and volume phase transition of polyelectrolyte gels, Journal of Applied Mechanics 84 (2017) 051005. doi:10.1115/1.4036113.

[37] A. D. Drozdov, A. A. Papadimitriou, J. H. Liely, C. G. Sanporean, Constitutive equations for the kinetics of swelling of hydrogels, Mechanics of Materials (2016). doi:10.1016/j.mechmat.2016.08.012.

[38] J. Hua, M. K. Mitra, M. Muthukumar, Theory of volume transition in polyelectrolyte gels with charge regularization, Journal of Chemical Physics 136 (2012) 134901. doi:10.1063/1.3698168.

[39] P. J. Flory, Thermodynamics of high polymer solutions, The Journal of Chemical Physics 10 (1942) 51–61. doi:10.1063/1.1723621.

[40] M. L. Huggins, Some properties of solutions of long-chain compounds., The Journal of Physical Chemistry 46 (1942) 151–158. doi:10.1021/j150415a018.

[41] B. Stinner, B. Nestler, H. Garcke, A diffuse interface model for alloys with multiple components and phases, SIAM Journal on Applied Mathematics 64 (2004) 775–799. doi:10.1137/S0036139902413143.

[42] A. Onuki, S. Puri, Spinodal decomposition in gels, Phys. Rev. E 59 (1999) R1331–R1334. doi:10.1103/PhysRevE.59.R1331.

[43] K.-A. Wu, P. K. Jha, M. Olvera de la Cruz, Pattern selection in polyelectrolyte gels by nonlinear elasticity, Macromolecules 45 (2012) 6652–6657. doi:10.1021/ma301549q.

[44] W. Hong, X. Wang, A phase-field model for systems with coupled large deformation and mass transport, Journal of the Mechanics and Physics of Solids 61 (2013) 1281 – 1294. doi:10.1016/j.jmps.2013.03.001.

[45] M. E. Gurtin, Generalized Ginzburg-Landau and Cahn-Hilliard equations based on a microforce balance, Physica D: Nonlinear Phenomena 92 (1996) 178 – 192. doi:10.1016/0167-2789(95)00173-5.

[46] A. D. Drozdov, J. deClaville Christiansen, C.-G. Sanporean, Inhomogeneous swelling of ph-responsive gels, International Journal of Solids and Structures 87 (2016) 11 – 25. doi:10.1016/j.ijsolstr.2016.02.037.

[47] M. G. Hennessy, A. Münch, B. Wagner, Phase separation in swelling and deswelling hydrogels with a free boundary, Phys. Rev. E 101 (2020) 032501. doi:10.1103/PhysRevE.101.032501.

[48] B. D. Coleman, W. Noll, The thermodynamics of elastic materials with heat conduction and viscosity, Archive for Rational Mechanics and Analysis 13 (1963) 167–178. doi:10.1007/BF01262690.

[49] R. M. Bowen, Part i - theory of mixtures, in: A. C. Eringen (Ed.), Continuum Physics, Academic Press, 1976, pp. 1–127. doi:10.1016/B978-0-12-240803-8.50017-7.

[50] H. Brenner, Kinematics of volume transport, Physica A: Statistical Mechanics and its Applications 349 (2005) 11–59. doi:10.1016/J.PHYSA.2004.10.033.

[51] J. Kim, J. Lowengrub, Phase field modeling and simulation of three-phase flows, Interfaces and Free Boundaries 7 (2005) 435–466. doi:10.1016/j.jcp.2016.05.016.

[52] Y. Mori, H. Chen, C. Micek, M.-C. Calderer, A dynamic model of polyelectrolyte gels, SIAM Journal on Applied Mathematics 73 (2013) 104–133. doi:10.1137/110855296.

[53] J. J. Feng, Y.-N. Young, Boundary conditions at a gel-fluid interface, Physical Review Fluids 5 (2020) 124304.

[54] M. G. Hennessy, G. Celora, A. Münch, B. Wagner, S. Waters, The electric double layer at the interface between a polyelectrolyte gel and solvent bath, Submitted (2021).

[55] M. Doi, Gel dynamics, Journal of the Physical Society of Japan 78 (2009) 052001. doi:10.1143/JPSJ.78.052001.

[56] T. K. Sherwood, R. L. Pigford, C. R. Wilke, Mass transfer, McGraw-Hill Book Co, New York, 1975.

[57] A. Logg, K.-A. Mardal, G. N. Wells, et al., Automated Solution of Differential Equations by the Finite Element Method, Springer, 2012. doi:10.1007/978-3-642-23099-8.

[58] I. Ohmine, T. Tanaka, Salt effects on the phase transition of ionic gels, The Journal of Chemical Physics 77 (1982) 5725–5729. doi:10.1063/1.443780.

[59] G. L. Celora, M. G. Hennessy, A. Münch, B. Wagner, S. L. Waters, The dynamics of a collapsing polyelectrolyte gel, arXiv (2021). arXiv:2105.06495.

[60] T. Shen, J. Kan, E. Benet, F. J. Vernerey, On the blistering of thermo-sensitive hydrogel: the volume phase transition and mechanical instability, Soft Matter 15 (2019) 5842–5853. doi:10.1039/C9SM00911F.

[61] M. Shibayama, K. Nagai, Shrinking kinetics of poly (N-isopropylacrylamide) gels T-jumped across their volume phase transition temperatures, Macromolecules 32 (1999) 7461–7468. doi:10.1021/ma990719v.

[62] B. Barrière, K. Sekimoto, L. Leibler, Peristaltic instability of cylindrical gels, The Journal of Chemical Physics 105 (1996) 1735–1738. doi:10.1063/1.472544.

[63] R. Veltz, BifurcationKit.jl, 2020. URL: https://hal.archives-ouvertes.fr/hal-02902346.

[64] N. Gavish, I. Versano, A. Yochelis, Spatially localized self-assembly driven by electrically charged phase separation, SIAM Journal on Applied Dynamical Systems 16 (2017) 1946–1968. doi:10.1137/16M1105876.

[65] N. Gavish, A. Yochelis, Theory of Phase Separation and Polarization for Pure Ionic Liquids, Journal of Physical Chemistry Letters 7 (2016) 1121–1126. doi:10.1021/ACS.JPCLETT.6B00370.

[66] K. R. Rajagopal, A. R. Srinivasa, On thermomechanical restrictions of continua, Proc. R. Soc. Lond. A. 460 (2004) 631–651. doi:10.1098/rspa.2002.1111.

[67] L. Onsager, Reciprocal relations in irreversible processes. i., Phys. Rev. 37 (1931) 405–426. doi:10.1103/PhysRev.37.405.

[68] S. L. Xue, B. Li, X. Q. Feng, H. Gao, A non-equilibrium thermodynamic model for tumor extracellular matrix with enzymatic degradation, Journal of the Mechanics and Physics of Solids 104 (2017) 32 – 56. doi:10.1016/j.jmps.2017.04.002.

[69] S.-L. Xue, S.-Z. Lin, B. Li, X.-Q. Feng, A nonlinear poroelastic theory of solid tumors with glycosaminoglycan swelling, Journal of Theoretical Biology 433 (2017) 49 – 56. doi:10.1016/j.jtbi.2017.08.021.

[70] A. Katchalsky, P. Curran, Nonequilibrium thermodynamics in biophysics, Books in Biophysics, Harvard University Press, 1965.

[71] S. R. d. Groot, Non-equilibrium thermodynamics, North-Holland series in physics, North-Holland, Amsterdam, 1962.

[72] F. G. Donnan, The Theory of Membrane Equilibria., Chemical Reviews 1 (1924) 73–90. doi:10.1021/cr60001a003.

[73] J. M. Huyghe, J. D. Janssen, Quadriphasic mechanics of swelling incompressible porous media, International Journal of Engineering Science 35 (1997) 793–802. doi:10.1016/S0020-7225(96)00119-X.